

DISSECTING THE RED SEQUENCE—III. MASS-TO-LIGHT VARIATIONS IN 3D FUNDAMENTAL PLANE SPACE

GENEVIEVE J. GRAVES^{1,2,3} & S. M. FABER¹

Draft version October 31, 2018

ABSTRACT

The Fundamental Plane of early type galaxies is observed to have finite thickness and to be tilted from the virial relation. Both of these represent departures from the simple assumption that dynamical mass-to-light ratios (M_{dyn}/L) are constant for all early type galaxies. We use a sample of 16,000 quiescent galaxies from the Sloan Digital Sky Survey to map out the variations in M_{dyn}/L throughout the 3D Fundamental Plane space defined by velocity dispersion (σ), effective radius (R_e), and effective surface brightness (I_e). Dividing M_{dyn}/L into multiple components allows us to separately consider the contribution to the observed M_{dyn}/L variation due to stellar population effects, IMF variations, and variations in the dark matter fraction within one R_e . Along the FP, we find that the stellar population contribution given some constant IMF ($M_{\star,IMF}/L$) scales with σ such that $M_{\star,IMF}/L \propto f(\sigma)$. Meanwhile, the dark matter and/or IMF contribution ($M_{dyn}/M_{\star,IMF}$) scales with M_{dyn} such that $M_{dyn}/M_{\star,IMF} \propto g(M_{dyn})$. This means that the two contributions to the tilt of the FP rotate the plane around different axes in the 3D space. The observed tilt of the FP requires contributions from both, with dark matter/IMF variations likely comprising the dominant contribution. Looking at M_{dyn}/L variations through the *thickness* of the FP, we find that M_{dyn}/L variations must be dominated either by IMF variations or by real differences in dark matter fraction with R_e . This means that the finite thickness of the FP is due to variations in the stellar mass surface density within R_e ($\Sigma_{\star,IMF}$), not the fading of passive stellar populations and it therefore represents genuine structural differences between early type galaxies. These structural variations are correlated with galaxy star formation histories such that galaxies with higher $M_{dyn}/M_{\star,IMF}$ have higher [Mg/Fe], lower metallicities, and older mean stellar ages. We discuss several physical mechanisms that might explain the observed co-variation between $M_{dyn}/M_{\star,IMF}$ and galaxy star formation histories. It is difficult to explain the observed enhancement of α -elements in lower-surface-brightness galaxies by allowing the IMF to vary. Differences in dark matter fraction can be produced by variations in the “conversion efficiency” of baryons into stars or by the redistribution of stars and dark matter through dissipational merging. The former explanation, specifically a model in which some galaxies experience low conversion efficiencies due to premature truncation of star formation, provides a more natural explanation for the co-variation of $M_{dyn}/M_{\star,IMF}$ and the observed stellar population properties.

Subject headings: galaxies: elliptical and lenticular, galaxies: structure, galaxies: evolution

1. INTRODUCTION

Early type galaxies are observed to obey many scaling relations among their structural properties. Early work identified a number of 1D relations, such as the Faber-Jackson relation between galaxy luminosity (L) and velocity dispersion (σ) (Faber & Jackson 1976), variations in galaxy mass-to-light ratio (M/L) versus L (Tinsley 1981; Faber et al. 1987), and various correlations of σ and L with galaxy effective radius (R_e) and effective surface brightness (μ_e) (Kormendy 1985), or with galaxy core radius (r_c) and central surface brightness (I_0) (Lauer 1985).

These relations generally reflect a 1D mass sequence of galaxies. It is clear however that early type galaxies comprise at least a two-parameter family in terms of their structure. In the three-dimensional parameter space of galaxy properties defined by σ , R_e , and surface brightness (expressed as μ_e in magnitudes or as I_e in lin-

ear flux units), early type galaxies populate a relatively tight two-dimensional plane, known as the Fundamental Plane (FP, Djorgovski & Davis 1987; Dressler et al. 1987). Projections of the FP appear narrow in some orientations, leading to the seemingly 1D relations listed above.

The FP can be understood as a manifestation of the virial plane predicted for relaxed systems, under the assumption that galaxy mass-to-light ratios (M_{dyn}/L) are constant (or at least smoothly varying) for all galaxies. If M_{dyn}/L were strictly constant and if structures were homologous for all early type galaxies, the FP would be equivalent to the virial plane, which takes the form $R_e \propto \sigma^2 I_e^{-1}$, and would be infinitely thin. Instead, the FP is rotated from the virial plane (e.g., Dressler et al. 1987; Djorgovski & Davis 1987). Jørgensen et al. (1996) find $R_e \propto \sigma^{1.24} I_e^{-0.82}$ for the FP of local cluster early type galaxies, as measured in the Gunn r band. In addition, the FP has finite thickness (e.g., Jørgensen et al. 1996; Forbes et al. 1998; Wuyts et al. 2004; Hyde & Bernardi 2009; Gargiulo et al. 2009) indicating further departures from a single virial plane. The “tilt” of the FP and its finite thickness indicate departures from the simplistic

¹ UCO/Lick Observatory, Department of Astronomy and Astrophysics, University of California, Santa Cruz, CA 95064, USA

² Department of Astronomy, University of California, Berkeley, CA 94720, USA; graves@astro.berkeley.edu

³ Miller Fellow

assumption that M_{dyn}/L is constant for all early type galaxies and that their structures are homologous.

This is the third in a series of four papers that explores the mapping between the 2D family of early type galaxy stellar populations and their structural properties. The first three papers in the series systematically gather together a number of galaxy properties that vary through the different dimensions of galaxy parameter space. Graves et al. (2009a, hereafter Paper I) showed that stellar populations vary differently as functions of σ than as functions of L . This systematic variation suggests an underlying multi-dimensional parameter space. Graves et al. (2009b, hereafter Paper II) mapped out the second dimension of stellar population properties in 3D Fundamental Plane space and correlated stellar population variations with FP parameters. In this paper, we focus on the corresponding mass-to-light ratios and how they relate to the distribution of galaxies in FP space.

We show here that the stellar population variations measured in Paper II do not provide enough variation in galaxy mass-to-light ratios to explain either the tilt or the thickness of the FP. Some correlated variation is also required in either the initial mass function (IMF) with which galaxies form their stars, or in the dark matter fraction inside R_e . At the same time, these variations are a key component of structural differentiation in galaxies that must also be related to their star formation histories. The results of these first three papers are gathered together in Paper IV (Graves et al. 2010, submitted to ApJ), which uses them to propose scenarios for galaxy formation and evolution through the thickness of the FP.

Section 2 briefly outlines the sample of galaxies used in this work, as well as our methods for grouping together similar galaxies to produce high signal-to-noise spectra that span the space of galaxy properties. In section 3, we discuss the various physical mechanisms that may contribute to the observed variations in M_{dyn}/L throughout the FP. Some of this variation is due to stellar population effects, but quantifying these depends critically on the stellar population models used to measure stellar mass-to-light ratios ($M_{*,IMF}/L$). We therefore investigate multiple ways of measuring $M_{*,IMF}/L$ from stellar population models in section 4. This comparison allows us to explore the range of possible $M_{*,IMF}/L$ values for our sample galaxies and to understand the biases inherent in each model. We demonstrate that, regardless of which method is chosen to measure $M_{*,IMF}/L$, the observed stellar population variations are inadequate to explain either the tilt or the thickness of the FP. Section 5 shows that the two contributions to the FP tilt (1: from known stellar population variations and 2: from IMF and/or dark matter fraction variations within R_e) rotate the plane around different axes in 3D Fundamental Plane space. It also investigates the various contributions to the *thickness* of the FP and shows that the spread in M_{dyn}/L through the plane is due primarily to the second factor: variations in the IMF and/or dark matter fractions. Section 6 discusses physical models that may produce the observed correlations between dark matter fraction or IMF variation and galaxy star formation histories. It illustrates that the observed trends can be explained by a model in which some galaxies experience low “conversion efficiency” turning baryons into stars due to truncated star formation histories. Finally, section 7 sum-

marizes our conclusions.

2. DATA

The data used in this analysis are the same as those used in Papers I and II. They consist of a sample of $\sim 16,000$ non-star-forming (quiescent) galaxies chosen from the SDSS spectroscopic Main Galaxy Sample (Strauss et al. 2002) in a relatively narrow redshift range. The sample selection is described in detail in Paper I.

Briefly, we construct a sample of quiescent galaxies by requiring that their spectra contain no detectable emission in either H α or the [OII] λ 3727 doublet (all measured line strengths are below a 2σ detection threshold)⁴, based on the emission line measurements of Yan et al. (2006) for SDSS Data Release 4 (DR4, Adelman-McCarthy et al. 2006) galaxies. We further limit the sample to a relatively narrow redshift slice ($0.04 < z < 0.08$) and to galaxies with light profiles consistent with early type morphologies. These criteria produce a sample of galaxies that fall on the red sequence in a color-magnitude diagram (see Figure 1 of Paper I), and which typically have bulge-dominated morphologies.

The various FP parameters are obtained for all galaxies in the sample, as follows. Photometry and R_e values are from de Vaucouleurs fits to the light profile. The radii and σ values are downloaded from the SDSS Catalog Archive Server⁵ and the apparent photometry from the NYU Value-Added Galaxy Catalog (Blanton et al. 2005). The photometry is subsequently corrected for Galactic extinction (Schlegel et al. 1998), K-corrected to the V-band at $z = 0$ using the IDL code *kcorrect* v4.1.4 (Blanton & Roweis 2007), and converted to absolute luminosities assuming a standard Λ CDM cosmology with $\Omega_\Lambda = 0.7$, $\Omega_M = 0.3$, and $h_0 = 0.7$. Both L and R_e have been corrected for known problems with the SDSS pipeline sky-subtraction around bright galaxies, as described in Paper I. The surface brightness I_e is then computed as $I_e = L_V/2\pi R_e^2$. All surface brightnesses and luminosities used in this work are measured in the V-band. The σ values are aperture-corrected to a constant $R_e/8$ aperture following Jørgensen et al. (1995) and Bernardi et al. (2003a). Spectra for the sample galaxies were downloaded from the SDSS Data Archive Server⁶.

The individual SDSS spectra of our galaxies typically have $S/N \sim 20 \text{ \AA}^{-1}$, while accurate stellar population analysis requires $S/N \geq 100 \text{ \AA}^{-1}$ (Cardiel et al. 1998). It is possible to make estimates of galaxy stellar population properties from individual SDSS spectra (e.g., Gallazzi et al. 2005) but we have chosen to take a different approach by defining bins that group together “similar” galaxies, then stacking the spectra of all galaxies in each bin to produce high S/N mean spectra that track the average properties of galaxies throughout the binning space. The ideal $S/N > 100 \text{ \AA}^{-1}$ requires ~ 25 galaxies

⁴ This emission cut excludes known star-forming galaxies and also LINER hosts. The LINER hosts can be considered quiescent systems, in the sense that they do not contain ongoing star formation, but they have systematically younger stellar populations (Graves et al. 2007) and have larger corrections to H β for emission inflill. We will return to LINERs in a future paper.

⁵ <http://cas.sdss.org/dr6/en/>

⁶ <http://das.sdss.org/DR6-cgi-bin/DAS>

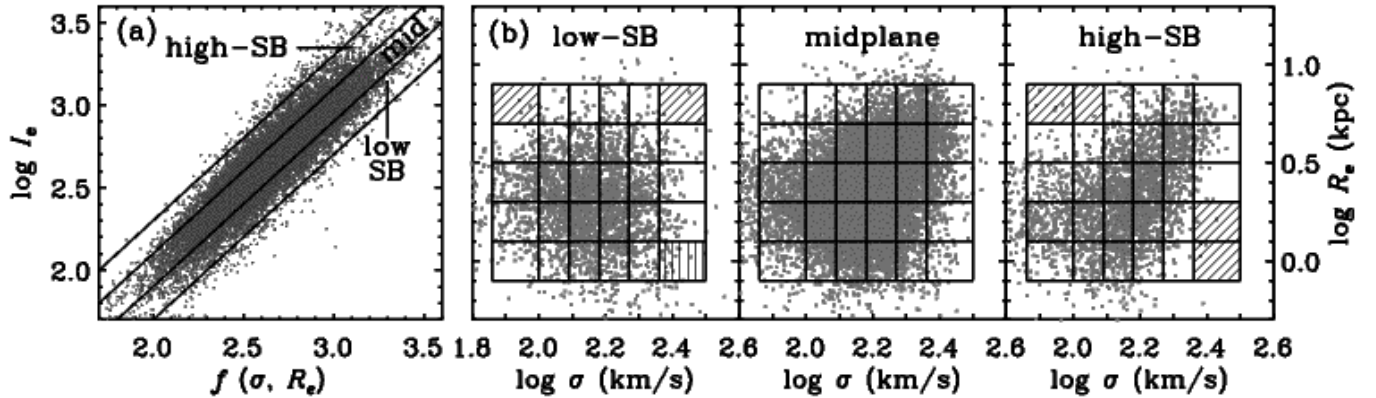


Figure 1. Sorting and binning galaxies in 3D FP space. (a) An edge-on view of the best fit to the FP, using a least-squares fit of I_e onto R_e and σ , which gives $f(\sigma, R_e) = 1.16 \log \sigma - 1.21 \log R_e + 0.55$. We divide the FP into three slices based on surface brightness residuals ($\Delta \log I_e$) to define low-surface-brightness, midplane, and high-surface-brightness slices. (b) Within each slice, galaxies are further divided into 6 bins in $\log \sigma$ and 5 bins in $\log R_e$, as illustrated. Diagonal shading indicates the six bins that do not contain enough galaxies to produce robust mean spectra and are therefore excluded from our analysis. Vertical shading indicates a bin where stellar population ages cannot be reliably measured (see Paper II).

per bin, depending on the S/N of the individual spectra that go into the composite.

In the analysis presented here, we use two different binning strategies to explore mass-to-light ratio variations along the FP and through its thickness. The first binning scheme is the one used in Paper II, which sorts and bins galaxies in the 3D parameter space defined by σ , R_e , and ΔI_e .⁷ This parameter space is ideal for studying trends in galaxy properties along a (nearly) face-on projection of the FP itself. The edge-on projection of this plane is shown in Figure 1a. We divide FP space into three slices based on residuals from the FP in the I_e dimension ($\Delta \log I_e$). These include a “midplane” slice, as well as high- and low-surface-brightness slices above and below the plane. We then define a 6×5 grid in $\log \sigma$ and $\log R_e$ within each slice (Figure 1b). Bin widths in $\log \sigma$, $\log R_e$ and $\log \Delta I_e$ (0.09 dex, 0.20 dex, and 0.10 dex, respectively) are substantially larger than the uncertainties in the measured quantities (typically ~ 0.04 dex, ~ 0.02 dex, and ~ 0.03 dex, respectively) so that the assignment of a galaxy to a given bin is relatively robust. We exclude bins that include fewer than 10 galaxies and/or have composite spectra with $S/N < 50 \text{ \AA}^{-1}$ (shaded regions in Figure 1b).

In §5.2 we examine trends through the *thickness* of the FP. For this section, we bin galaxies in a 2D binning space defined by σ and ΔI_e only. In Figure 2, we show the distribution of the sample galaxies in σ – ΔI_e space, which is essentially a cross-section projected through the thickness of the FP. We define a 6×5 grid in this space and use it to sort galaxies into bins through the FP cross-section. Bins in σ are chosen to be consistent with the 3D binning scheme of Figure 1. Bins in ΔI_e span the majority of the data; the bin width is chosen such that at high σ , even the outlying ΔI_e bins contain > 20 galaxies and produce stacked spectra with $S/N > 100 \text{ \AA}^{-1}$. This binning scheme means that galaxies with a variety of

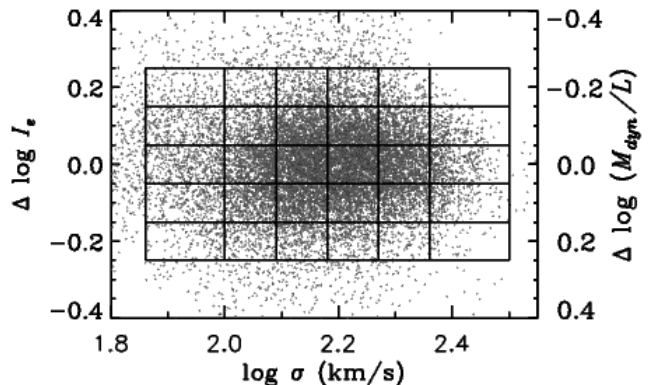


Figure 2. Sorting and binning galaxies through the thickness of the FP. The quantity $\Delta \log I_e$ is defined as in Figure 1a. We sort the sample into the same 6 bins in σ as in Figure 1b, and further into 5 bins in $\Delta \log I_e$.

R_e values are combined together in each bin. However, as shown in Paper II, the stellar population properties and therefore the star formation histories of quiescent galaxies do not depend on R_e at fixed σ .

With ΔI_e defined in this way, there is a direct correspondence between I_e variations and variations in M_{dyn}/L . Recall that $M_{dyn}/L \propto \sigma^2 R_e / I_e R_e^2 \propto \sigma^2 / I_e R_e$. Variations in I_e are defined at fixed points in σ and R_e . Thus variations in I_e at fixed values of σ and R_e correspond to variations in M_{dyn}/L , such that $\Delta I_e \propto \Delta(M_{dyn}/L)^{-1}$.

Once the galaxies have been sorted into bins, the spectra of all galaxies in each bin are stacked together using an algorithm that masks areas around bright sky lines and rejects highly deviant pixels. We measure the full set of Lick indices in the resulting mean spectra, then use them to model the mean stellar population properties of the galaxies in each bin using the single burst population models of Schiavon (2007) and the code EZ_Ages, described in Graves & Schiavon (2008). Sections 4.2–4.4 of Paper I give a detailed description of this process.

There is one significant difference between the data presented here and those of Paper II: here the stacked galaxy spectra have been corrected for small quantities

⁷ For brevity, we will use the terms σ , R_e and ΔI_e throughout this paper to refer to the various dimensions of FP space. It should be understood that all bins are defined in log space (i.e., $\log \sigma$, $\log R_e$, and $\Delta \log I_e$) and that we always measure each quantity in logarithmic units.

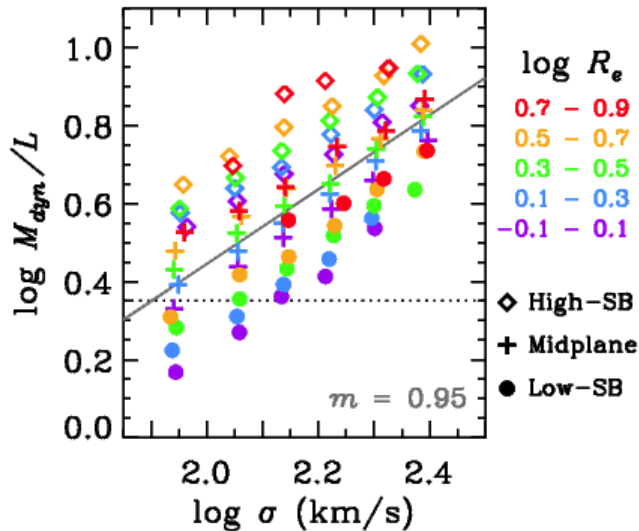


Figure 3. Median values of σ and M_{dyn}/L for each bin of galaxies (3D FP binning). The listed values of R_e are in kpc. The solid line shows a least-squares fit of M_{dyn}/L onto σ for galaxies on the FP midplane, with the slope of the relation indicated in the lower right corner. If the FP and the virial plane were equivalent, M_{dyn}/L would be constant for all galaxies. Instead, there is a strong increase in M_{dyn}/L as σ increases (the “ σ tilt” of the FP) and a substantial spread in M_{dyn}/L at fixed σ and R_e (the “thickness” of the FP).

of emission infill in the $H\beta$ absorption line used to determine ages, as described in Appendix A. The quantity of emission infill is similar in the various stacked spectra. Therefore the main effect of this correction is to systematically lower the derived ages by ~ 0.12 dex and to raise $[Fe/H]$ values by ~ 0.06 dex compared to Paper II.

3. PHYSICAL EFFECTS THAT CONTRIBUTE TO M_{DYN}/L VARIATIONS THROUGHOUT THE FUNDAMENTAL PLANE

As discussed above, both the tilt of the FP and its finite thickness represent departures from the simple assumption of constant M_{dyn}/L . This is illustrated in Figure 3 for the galaxies in our sample, which span almost an order of magnitude in M_{dyn}/L . The systematic variation of M_{dyn}/L with σ is a 2D projection of the 3D “tilt” of the FP. This σ -component to the FP tilt has a slope of $M_{dyn}/L \propto \sigma^{0.95}$ in the data presented here, based on a least squares fit that weights each binned data point by the number of galaxies in the bin. The tilt of the FP is typically parameterized as a function of M_{dyn} , but it is sometimes useful to discuss the σ component of the tilt separately (as in §5.1, where we show that the stellar population contribution to the tilt is purely a function of σ). Throughout this paper, we will use the term “ σ tilt” to discuss mass-to-light variation along the FP as a function of σ and the term “total tilt” to describe variation along the FP as a function of M_{dyn} .

In addition to the σ tilt shown in Figure 3, M_{dyn}/L also varies significantly at fixed σ . This variation is dominated by differences in ΔI_e through the thickness of the FP (different symbols in Figure 3), although M_{dyn}/L also varies with R_e at fixed σ (different colors in Figure 3).

The FP appears to be the same in all environments (Kochanek et al. 2000; de la Rosa et al. 2001; de Carvalho et al. 2003; Reda et al. 2005, but see

Bernardi et al. 2003b) and includes both elliptical and S0 galaxies on the same plane (Jørgensen et al. 1996; Fritz et al. 2005). The slope of the FP evolves with redshift, consistent with the passive aging of the stellar populations (e.g., Kelson et al. 1997; Jørgensen et al. 1999; Bernardi et al. 2003b; van de Ven et al. 2003; Holden et al. 2005; Jørgensen et al. 2006; van der Marel & van Dokkum 2007) or with passive evolution plus a small quantity of residual star formation (Gebhardt et al. 2003), but the thickness of the FP is constant out to $z \sim 0.6$ (Kelson et al. 1997; Jørgensen et al. 1999; Treu et al. 2001). Thus the tilt of the FP appears to be time-dependent but the thickness of the FP does not, suggesting that these two departures from constant M_{dyn}/L may be driven by different mechanisms.

A number of different physical processes can contribute to the variations in M_{dyn}/L that produce the tilt and thickness of the FP. These include differences in the dynamical structure of galaxies, variations in the ratio of dark matter to stellar mass, variations in the initial mass function (IMF) with which galaxies form their stars, and difference in the stellar mass-to-light ratios due to the star formation rates, ages and metallicities of the galaxies.

To elucidate the contributions of each of these physical processes, we separate the quantity M_{dyn}/L into four components as follows:

$$\frac{M_{dyn}}{L} = \frac{M_{dyn}}{M_{tot}} \times \frac{M_{tot}}{M_{\star}} \times \frac{M_{\star}}{M_{\star,IMF}} \times \frac{M_{\star,IMF}}{L}, \quad (1)$$

where M_{dyn} is the dynamical mass estimate for the galaxy given by $M_{dyn} \equiv 5\sigma^2 R_e/G$ (e.g., Cappellari et al. 2006), M_{tot} is the total mass of the galaxy inside R_e , M_{\star} is the true stellar mass of the galaxy inside R_e , $M_{\star,IMF}$ is the estimated stellar mass inside R_e assuming some constant IMF, and L is the V -band luminosity inside R_e (all quantities include L are projected within R_e). With these definitions, the components of equation 1 represent the following physical properties:

- M_{dyn}/M_{tot} is the “dynamical structure term.” This accounts for any discrepancies between the simple dynamical mass estimator and the total projected mass within R_e .
- M_{tot}/M_{\star} is the “dark matter term.” It accounts for differences between the total projected mass within R_e and the projected luminous stellar mass within R_e .
- $M_{\star}/M_{\star,IMF}$ is the “IMF term.” It accounts for differences between the true projected stellar mass inside R_e and the projected stellar mass computed with an assumed initial mass function. If the true IMF matches the IMF used in the stellar population modelling, $M_{\star}/M_{\star,IMF} = 1$.
- $M_{\star,IMF}/L$ is the “stellar population term.” It accounts for the stellar mass-to-light ratio, given an assumed IMF. The stellar population term can be estimated from the mean stellar age, the mean metallicity, and the star formation history of the galaxy.

Unfortunately, not all of these components can be determined observationally. For the SDSS data used in this analysis, only M_{dyn} , $M_{*,IMF}$, and L are measurable quantities. In practice, M_* can only be robustly determined for resolved stellar systems. M_* values quoted for unresolved stellar systems *always* rely upon stellar population modelling plus the assumption of a single, constant IMF. They are therefore really values of $M_{*,IMF}$, not a true measurement of M_* .

Direct measurements of M_{tot} are only possible where an independent mass estimated can be derived. Recent examples include resolved kinematic observations of nearby early type galaxies (Cappellari et al. 2006) and strong galaxy-galaxy lenses (Bolton et al. 2007, 2008; Koopmans et al. 2009) which show that the simple dynamical estimator does an excellent job of reproducing the galaxy masses derived from kinematics or lensing. These studies suggest that $M_{dyn} = M_{tot}$, with scatter of 0.06–0.07 dex standard deviation around the one-to-one relation (cf. Cappellari et al. 2006, Bolton et al. 2007). This level of variation in M_{dyn}/M_{tot} is clearly inadequate to explain the variation in M_{dyn}/L in Figure 3. These observational results are further supported by numerical simulations which show that galaxies with orbital anisotropies large enough to move them off the FP are dynamically unstable (Ciotti et al. 1996; Ciotti & Lanzoni 1997; Nipoti et al. 2002).

Assuming that $M_{dyn} = M_{tot}$ and bearing in mind that M_* is not a measurable quantity in unresolved stellar systems, equation 1 simplifies to

$$\frac{M_{dyn}}{L} = \frac{M_{dyn}}{M_{*,IMF}} \times \frac{M_{*,IMF}}{L}, \quad (2)$$

where both $M_{dyn}/M_{*,IMF}$ and $M_{*,IMF}/L$ are measurable quantities. Variations in $M_{*,IMF}/L$ are due to known stellar population effects, while variations in the quantity $M_{dyn}/M_{*,IMF}$ can be produced by variations either in the IMF or in the dark matter fraction inside R_e . Hereafter, we will refer to the $M_{dyn}/M_{*,IMF}$ term as the “dark matter/IMF” contribution with the understanding that variations in this term can be attributed to either effect, or to both in combination.

Many previous studies have indicated that the stellar population term ($M_{*,IMF}/L$) contributes not more than 1/2 of the observed FP tilt (e.g., Pahre et al. 1995; Prugniel & Simien 1997; Pahre et al. 1998; Scodreggio et al. 1998; Mobasher et al. 1999; Padmanabhan et al. 2004; Trujillo et al. 2004; Gallazzi et al. 2005; Jun & Im 2008; La Barbera et al. 2008; Hyde & Bernardi 2009, but see also Allanson et al. 2009 who find that using a single burst star formation history produces enough variation in $M_{*,IMF}/L$ to explain the full FP tilt). This then requires variations in $M_{dyn}/M_{*,IMF}$ due to variations in either the IMF (as proposed by Renzini & Ciotti 1993 and Chiosi et al. 1998) or in the dark matter fraction inside R_e (e.g., Renzini & Ciotti 1993; Pahre et al. 2001; Padmanabhan et al. 2004; Gallazzi et al. 2005; Hyde & Bernardi 2009) to produce the observed tilt of the FP.

The case for dark matter variation has recently gotten a boost from simulations of galaxy mergers that include gaseous dissipation. Several authors have shown that

the degree of dissipation during mergers determines the dark matter fraction within R_e in merger remnants (e.g., Robertson et al. 2006; Dekel & Cox 2006). Under realistic conditions in which mergers of more massive galaxies have decreasing amounts of gas, such simulations can reproduce the observed tilt of the FP (Kobayashi 2005; Robertson et al. 2006; Dekel & Cox 2006; Covington 2008; Hopkins et al. 2008a). A limited quantity of further dissipationless merging should preserve the tilted FP (Capelato et al. 1995; Dantas et al. 2003; Nipoti et al. 2003; Boylan-Kolchin et al. 2005; Robertson et al. 2006).

It seems therefore that, while stellar population effects may contribute to the tilt of the FP, further variation in the dark matter/IMF term are required. This paper shows that these two contributions to the FP tilt rotate the plane around different axes in the 3D space, such that $M_{*,IMF} \propto \sigma^{0.30}$, while $M_{dyn}/M_{*,IMF} \propto M_{dyn}^{0.24}$. We also show that dark matter/IMF variations are required to produce the *thickness* of the FP: stellar population effects contribute some, but the dominant component of variation must come from differences in the dark matter/IMF term.

4. MEASURING $M_{*,IMF}/L$

As discussed in section 3, the quantities M_{dyn} , $M_{*,IMF}$, and L are the only components of equation 1 that can be determined for the SDSS data. Of these, M_{dyn} and L are relatively direct measurements while $M_{*,IMF}$, the stellar mass estimate, comes from $L \times M_{*,IMF}/L$, where $M_{*,IMF}/L$ is determined through stellar population modelling. In Paper II, we measured the mean age, metallicity, and abundance patterns for the stacked spectra in 3D FP space. With these quantities determined, there are three remaining factors that affect $M_{*,IMF}/L$. These are:

1. The stellar population model code used to compute $M_{*,IMF}/L$.
2. The library of star formation histories used in the models.
3. Whether the stellar population modelling is done by fitting individual spectral absorption lines, or by fitting the broad-band galaxy spectral energy distributions (SEDs).

This section addresses how each of these factors affect the determination of $M_{*,IMF}/L$, in order to motivate our choice of models and to assess the extent to which our final conclusions depend upon this choice. Qualitatively, our conclusions turn out to be independent of the exact choice of stellar population model and star formation history used to determine $M_{*,IMF}/L$, although quantifying these relationships does depend on the choice of model.

Longhetti & Saracco (2009) have recently addressed the first issue listed above using a suite of stellar population models to predict $M_{*,IMF}/L$ based on optical and infra-red colors. They examine the dependence of $M_{*,IMF}/L$ on age, metallicity, the IMF, and the choice of stellar population model codes. They explore several popular model codes including those of Bruzual & Charlot (2003) and Maraston (2005), as well as PEGASE (Fioc & Rocca-Volmerange 1997), and GRASIL (Silva et al. 1998) and find that the different

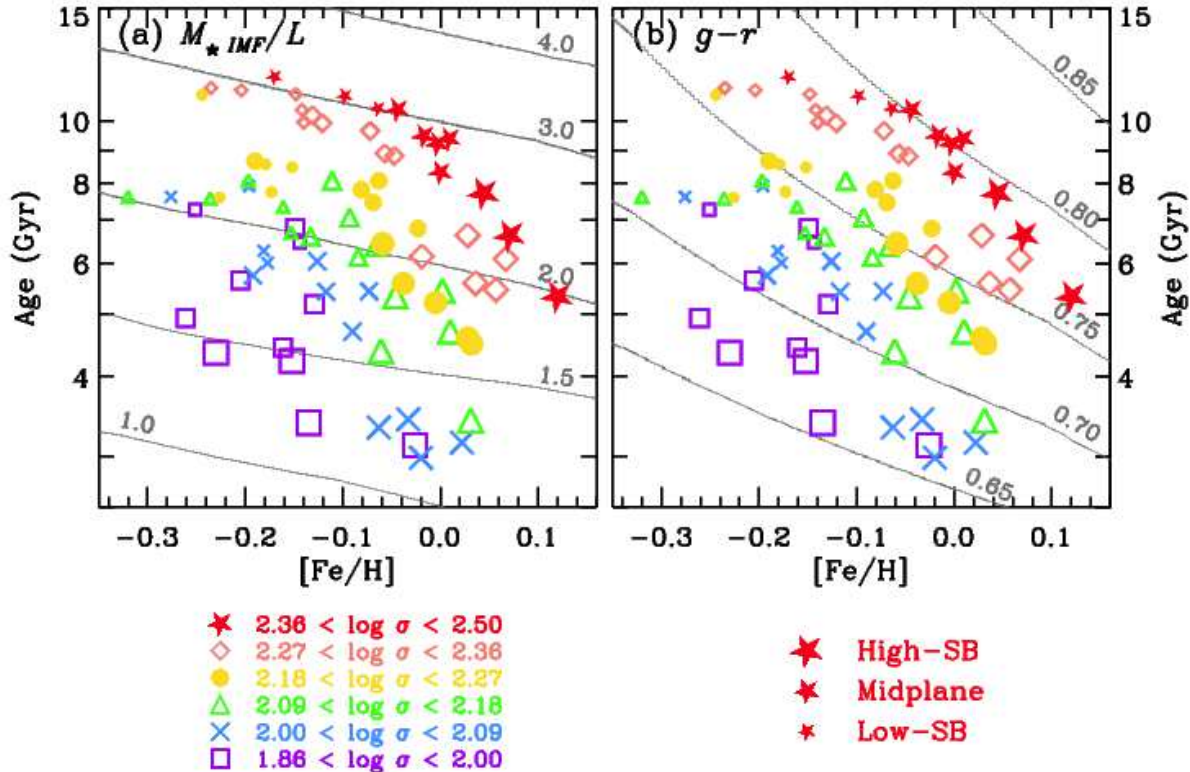


Figure 4. Age and [Fe/H] values measured in the stacked spectra (3D FP binning). Multiple symbols with the same size and color represent different values of R_e ; only bins with small errors ($\Delta[\text{Fe}/\text{H}] < 0.05$ dex and $\Delta\text{Age} < 15\%$) are shown. Galaxies with higher values of σ typically have older ages and higher [Fe/H] than galaxies with low values of σ . At fixed σ , galaxies with high (low) surface brightness have younger (older) ages and higher (lower) [Fe/H] than galaxies at the same σ that lie on the FP midplane (c.f., Paper II). Lines of constant $M_{*,IMF}/L$ (a) and lines of constant $g-r$ color (b) from BC03 models are overplotted as the gray lines. From a given value of age and [Fe/H], the corresponding value of $M_{*,IMF}/L$ and $g-r$ can be estimated. $M_{*,IMF}/L$ depends strongly on age but only weakly on [Fe/H], while $g-r$ depends strongly on both age and [Fe/H]. The anti-correlated variations in age and [Fe/H] at fixed σ move galaxies nearly along lines of constant $g-r$ but spread the galaxies over a range of $M_{*,IMF}/L$.

codes produce relatively consistent $M_{*,IMF}/L$ predictions.

If the ages and metallicities of the galaxies are known, Longhetti & Saracco (2009) find that the largest variations in $M_{*,IMF}/L$ determinations are due to the choice of IMF, with a zeropoint shift of ~ 0.26 dex between the Salpeter (1955) and Chabrier (2003) IMFs and of ~ 0.21 dex between the Salpeter and Kroupa (2001) IMFs, in the sense that the Salpeter IMF predicts larger values of $M_{*,IMF}/L$ than either Chabrier or Kroupa. Relative values of $M_{*,IMF}/L$ between different galaxies are robust to this effect, *as long as the IMF is the same for all galaxies*.

In the following sections, we examine the effects on $M_{*,IMF}/L$ of various star formation histories, and compare SED-based estimates of $M_{*,IMF}/L$ with those derived from spectral absorption features. All of the models presented here are based on isochrones computed for scaled-solar element abundance patterns.⁸

⁸ Since the galaxies presented here typically have super-solar [Mg/Fe], these are not an ideal match to the data. Mg-enhanced isochrones are shifted to cooler temperatures than scaled-solar isochrones, but a complicated interplay between different abundance effects makes it challenging to predict how various non-solar abundance patterns will affect $M_{*,IMF}/L$ (e.g., Dotter et al. 2007; Lee et al. 2010). Understanding these effects in detail may well represent the next major step forward in stellar population modelling.

4.1. Single Burst Models for $M_{*,IMF}/L$

As a reference point, we begin by computing our own values of $M_{*,IMF}/L$ using simple single-burst stellar population models (SSPs). Having mapped out the variations in mean age and metallicity through 3D FP space in Paper II, we are now in a position to study how these variations contribute to the observed variations in M_{dyn}/L . The modelling process is illustrated in Figure 4, which shows the values of mean, light-weighted age versus [Fe/H] determined from the stacked galaxy spectra, as described in Paper II. We have overlaid lines of constant stellar population mass-to-light ratio ($M_{*,IMF}/L$, panel a) and constant $g-r$ color (panel b) derived from the single burst stellar population models of Bruzual & Charlot (2003, hereafter BC03) with a Chabrier IMF. These curves make it possible to read off model values of $M_{*,IMF}/L$ and $g-r$ for each set of stacked spectra considered here.⁹

The different colors and symbols encode the σ values for each stacked spectrum, while the symbol size encodes

⁹ The BC03 models are computed for solar abundance ratios only, which is not an accurate reflection of the abundance pattern of our sample galaxies. Nevertheless, we show in Appendix B that the BC03 models, when chosen to match the SSP ages and [Fe/H] values from our stellar population modelling, are able to accurately reproduce the observed galaxy colors.

ΔI_e , as indicated. The plot includes the various bins in R_e but these are not differentiated in the figure, as neither age nor $[\text{Fe}/\text{H}]$ depend on R_e (see Paper II). The figure illustrates the main conclusion of Paper II: that the stellar populations of quiescent galaxies form a two-parameter family. The two dimensions of this family are such that galaxies with higher values of σ tend to have older ages and higher $[\text{Fe}/\text{H}]$ than galaxies with low σ , while at fixed σ galaxies with lower surface brightnesses have older ages and lower $[\text{Fe}/\text{H}]$ than those with higher surface brightnesses.

It is interesting to note that, although galaxies at fixed σ span a significant range in age and $[\text{Fe}/\text{H}]$, this variation moves them almost exactly along lines of constant $g-r$ color, as shown in Figure 4b. Thus, a process that attempts to use galaxy colors to model stellar populations will not successfully distinguish between the different populations at fixed σ . This is due to a nearly perfect alignment of the age-metallicity degeneracy in color with the measured anti-correlated of age and $[\text{Fe}/\text{H}]$ in galaxies at fixed σ . However, lines of constant $M_{\star, \text{IMF}}/L$ in Figure 4a follow shallower trajectories compared to lines of constant $g-r$ color, such that galaxies at fixed σ span a range of $M_{\star, \text{IMF}}/L$ values but not a range of colors. Using the full 5-band SDSS photometry does not give significantly improved $M_{\star, \text{IMF}}/L$ values, as all optical colors follow similar trajectories in age- $[\text{Fe}/\text{H}]$ space.¹⁰

The models shown here are based on single burst stellar population models (SSPs), which are almost certainly not accurate descriptions of the star formation histories of galaxies. However, such simple models are more transparent to interpret, and they provide a good reference point for considering models with more complicated star formation histories. Appendix B shows that the $g-r$ colors derived from Figure 4b do an excellent job of reproducing the observed galaxy colors, which gives us confidence that the derived values of $M_{\star, \text{IMF}}/L$ are likewise reasonable.

4.2. Models for $M_{\star, \text{IMF}}/L$ with Complex Star Formation Histories

For galaxies with old stellar populations, the differences between single burst values for $M_{\star, \text{IMF}}/L$ and those from extended star formation histories are small. However, galaxies with younger mean light-weighted ages may harbour a bright young sub-population obscuring a large population of older stars that contribute substantially to M_{\star} but very little to the integrated galaxy light. For these galaxies, the single burst estimates for younger galaxies are almost certainly too low.

This is illustrated in Figure 5a, which plots $M_{\star, \text{IMF}}/L$ against the $\text{H}\beta$ absorption line strength.¹¹ The figure compares single burst models (dashed line) to models with continuous star formation (solid line) that begins at $z = 10$, proceeds at a constant star formation rate, then is abruptly truncated at various times.¹² These star formation histories are indistinguishable for values

¹⁰ There is a slight steepening of the lines of constant color as colors become bluer (e.g., lines of constant $u-g$ are steeper than $g-r$) but even the reddest $i-z$ color is not nearly as flat as the lines of constant $M_{\star, \text{IMF}}/L$ in Figure 4.

¹¹ $\text{H}\beta$ is the major age discriminant used in the stellar population modeling of Paper II.

¹² In order to isolate the effect of age distribution in the stel-

of $\log(M_{\star, \text{IMF}}/L) > 0.35$, corresponding to single burst ages > 7 Gyr or constant star formation rates with truncation times $t_t > 3$ Gyr ago. At lower values of $M_{\star, \text{IMF}}/L$, single burst models can substantially underestimate $M_{\star, \text{IMF}}/L$ if the true star formation history is more extended.

In Figure 5c, we show $\text{H}\beta$ versus $M_{\star, \text{IMF}}/L$ for a set of exponentially declining star formation rates with e-folding time τ (so-called “ τ models”). For each τ , we compute a set of models in which the onset of star formation occurs at different times, spanning a range formation redshifts with $0.25 < z_f < 40$. However, the majority of the models with $\tau > 0.5$ imply $z = 0$ star formation rates that are too large for our quiescent galaxy sample. These are excluded from the set of viable models, as explained below.

The sample presented here includes only galaxies with $\text{H}\alpha$ emission-line fluxes below a 2σ detection threshold. We take the 2σ error value as an upper limit on the intrinsic $\text{H}\alpha$ flux for each galaxy, then convert this limit into a star formation rate following Kennicutt (1998, equation 2). Using the Gallazzi et al. (2005) measurements of $M_{\star, \text{IMF}}$ for each galaxy (explored in greater detail in §4.3), we compute an upper limit to the specific star formation rate (SSFR) for each sample galaxy. The vast majority (96%) of our sample galaxies have upper limits on their SSFRs that are below $0.1 M_{\odot} \text{ yr}^{-1}/10^{11} M_{\odot}$. We therefore use this value to restrict the set of τ models.

In Figure 5c, we show only models that have SSFRs at $z = 0$ that are less than $0.1 M_{\odot} \text{ yr}^{-1}/10^{11} M_{\odot}$. Low values of τ lead to models with short e-folding times, which closely resemble single burst star formation histories. At high values of τ , only models in which star formation begins at very early times have low enough SSFRs today to be included in the sample. The net effect is that the $M_{\star, \text{IMF}}/L$ values for a given observed $\text{H}\beta$ line strength are nearly identical to the single burst value, regardless of the values of τ or z_f . For τ -model star formation histories, single burst models in fact give a good approximation of the true value of $M_{\star, \text{IMF}}/L$.

However, models which include an abrupt truncation of star formation can have substantially different values of $M_{\star, \text{IMF}}/L$ for a given $\text{H}\beta$ line strength. In Figure 5d, we modify our library of τ models to include models that follow exponentially declining star formation histories that are suddenly truncated 1 Gyr before the time of observation. These models show some variation in $\text{H}\beta$ line strengths for a fixed value of $M_{\star, \text{IMF}}/L$, depending on the star formation history. The spread is modest for galaxies with $M_{\star, \text{IMF}}/L > 0.35$ but is larger for galaxies with lower $M_{\star, \text{IMF}}/L$.

Based on this suite of results, we infer that $M_{\star, \text{IMF}}/L$ values above 0.35 are relatively insensitive to the details of the galaxy star formation histories and are therefore reliable. In contrast, values of $M_{\star, \text{IMF}}/L$ below 0.35 may be off by 0.1–0.15 dex and are more likely to be skewed too low for the youngest galaxies with the lowest $M_{\star, \text{IMF}}/L$.¹³

lar populations, the constant star formation rate models, as well as the more complicated τ -models considered in this section, are computed at Solar metallicity.

¹³ It should be noted that these statements apply to *smoothly varying* star formation histories. Non-continuous (i.e., bursty) star

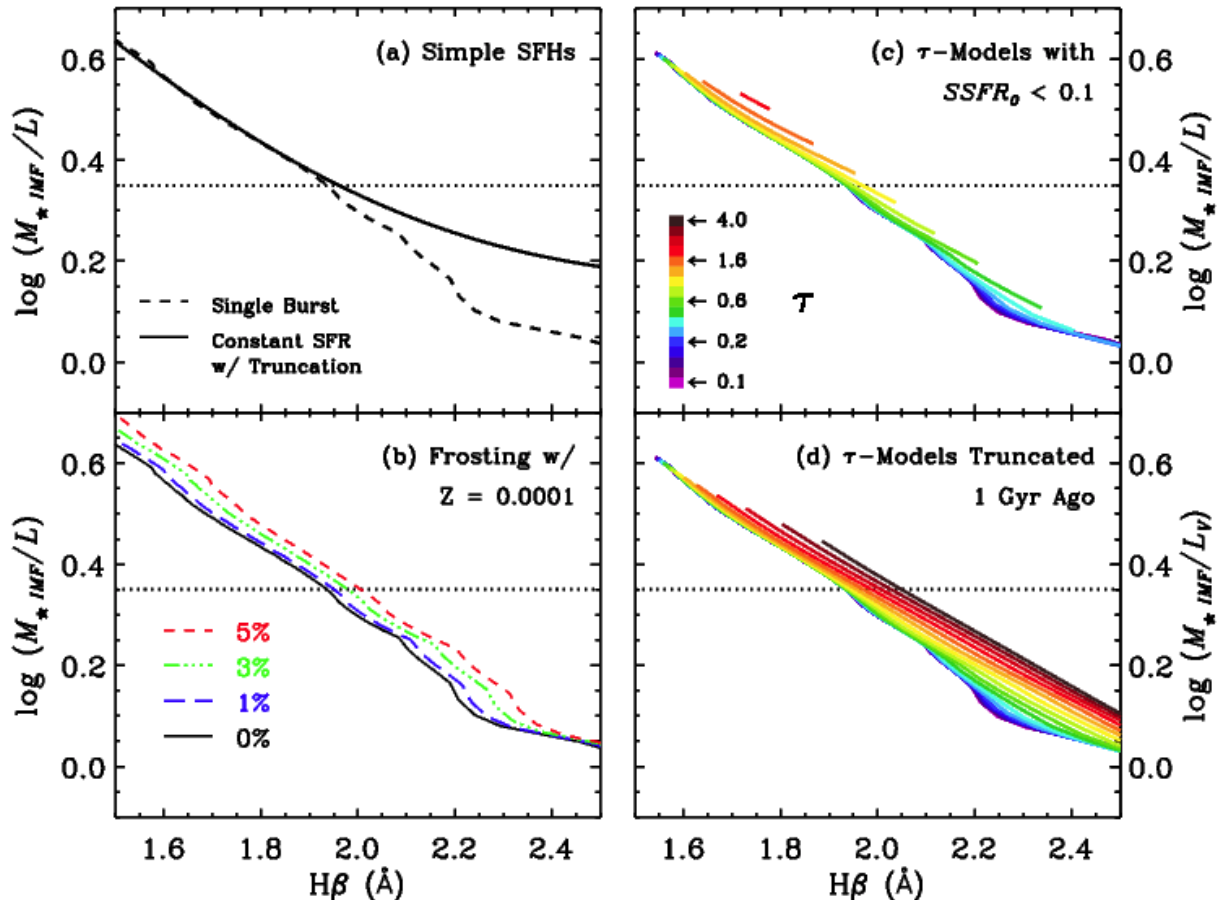


Figure 5. A comparison of $M_{*,IMF}/L$ values from models with different star formation histories. All models are BC03 models with a Chabrier IMF and solar abundances. (a) Simple star formation histories: the dashed line shows $M_{*,IMF}/L$ and $H\beta$ values from single burst star formation histories, while the solid line shows values from models with constant star formation that begins at $z = 10$ and truncates abruptly at various times. Differences in $M_{*,IMF}/L$ due to star formation history become relevant for $\log(M_{*,IMF}/L) < 0.35$, which corresponds to $t_{quench} = 3$ Gyr ago. (b) Models with a frosting of metal-poor ($Z = 0.0001$) stars, with fractions as indicated. Small, very metal-poor populations produce slightly higher $M_{*,IMF}/L$ for a given value of $H\beta$. (c) τ -models with $0.1 < \tau < 4.0$ Gyr and a range of initial formation redshifts ($0.25 < z_f < 40$). Only models with SSFRs consistent with our sample galaxies are shown ($< 0.1 M_{\odot} \text{ yr}^{-1}/10^{11} M_{\odot}$). These all have mass-to-light ratios consistent with the single burst models. (d) τ -models that have been abruptly truncated 1 Gyr before the time of observation. This family of models produces a limited range of $H\beta$ values for a given value of $M_{*,IMF}/L$, particularly for $\log(M_{*,IMF}/L) < 0.35$.

Finally, Maraston et al. (2009) have suggested that early type galaxies may contain a small sub-population of very metal-poor stars. They find that models for single-metallicity old stellar populations cannot match the color evolution of luminous red galaxies in the SDSS from $z = 0.7$ to $z = 0.1$. They demonstrate that adding a frosting (3% by mass) population of low metallicity ($Z = 0.0001$, i.e., $[\text{Fe}/\text{H}] = -2.2$) stars makes it possible to match the observed color evolution. In Figure 5b, we illustrate the effect of such a population on $M_{*,IMF}/L$ and $H\beta$. The 3% frosting population suggested by Maraston et al. (2009) results in $M_{*,IMF}/L$ values that are < 0.05 dex higher for a given observed values of $H\beta$, which is comparable to the variation produced by the τ -model star formation histories considered here.

formation histories can also produce substantially different values of $M_{*,IMF}/L$. However, in this analysis, we are examining stacks of many dozens of spectra, which means that the assumption of continuous star formation histories is reasonable. This is one benefit of stacking.

This leads to a key point. *In all cases, the single burst models give a lower limit on $M_{*,IMF}/L$.* Single burst models in fact give us a powerful tool because we can understand the biases in measurements based upon them. This gives us a benchmark against which to compare other, more complicated determinations of $M_{*,IMF}/L$ for which the biases are less clear.

4.3. $M_{*,IMF}/L$ from Spectral Absorption Lines vs. Optical Colors

Figure 6 compares $M_{*,IMF}/L$ from four different sets of authors, two of which are computed based on fits to spectral absorption features (Gallazzi et al. 2005 and Kauffmann et al. 2003b) and two of which are based on optical colors or multi-band photometry (Blanton & Roweis 2007 and Bell et al. 2003), to our benchmark single burst models. All four of these $M_{*,IMF}/L$ measurements are available for the individual SDSS galaxies used in our sample. Each papers' version of $M_{*,IMF}/L$ uses slightly different stellar population models and forms for the IMF. We have corrected the ze-

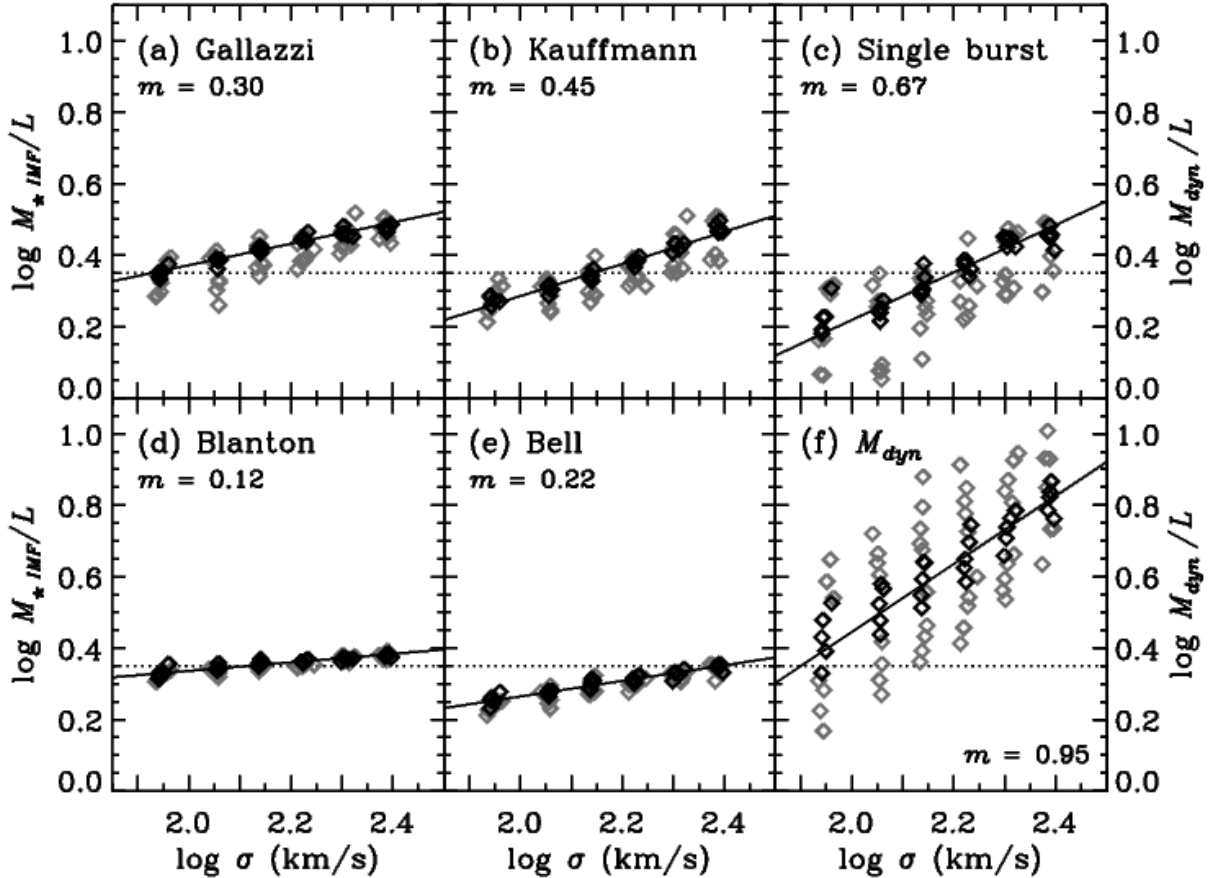


Figure 6. (a-e) Various estimates of $M_{*, IMF}/L$ for the galaxies in our sample as a function of σ . Galaxy bins on the FP midplane are shown in black, while those on the low- and high-SB slices are shown in gray. Panels (a-c) show values derived from spectral absorption features, including measurements from (a) Gallazzi et al. (2005), (b) Kauffmann et al. (2003b), and (c) our single burst values. Panels (d-e) show values based on fits to multi-band photometry, following the prescriptions of (d) Blanton & Roweis (2007) and (e) Bell et al. (2003). In each panel, solid lines show least squares fits of $M_{*, IMF}/L$ onto σ for the FP midplane galaxies only, weighted by the number of galaxies in each bin. The slopes are indicated in each panel. The dotted line at $M_{*, IMF}/L = 0.35$ marks the point below which differences in the star formation history significantly affect the determination of $M_{*, IMF}/L$ (see section 4.2). (f) The values of M_{dyn}/L from Figure 3 are reproduced for comparison. Regardless of the method used to measure $M_{*, IMF}/L$, it clearly cannot provide either the full slope of M_{dyn}/L with σ (the “ σ tilt” of the FP) nor the spread in M_{dyn}/L at fixed σ (the “thickness” of the FP).

repoints of the Kauffmann et al. (2003b) and Bell et al. (2003) values to match the Chabrier IMF assumed by the Gallazzi et al. (2005), Blanton & Roweis (2007), and our single burst models.

The Kauffmann et al. (2003b) and Gallazzi et al. (2005) stellar mass estimates for the individual SDSS galaxies were downloaded from the derived data catalogs from SDSS studies at MPA/JHU¹⁴. Kauffmann et al. (2003b) determine $M_{*, IMF}/L$ by fitting the D_n4000 (Balogh et al. 1999) and $H\delta_A$ (Worthey & Ottaviani 1997) spectral features to a library of models. Their model star formation histories comprise a set of exponentially declining star formation rates with varying τ , a range of total metallicities (always with the solar abundance pattern), and superposed random bursts of star formation at late times. We have corrected the Kauffmann et al. stellar mass measurements from SDSS Petrosian magnitudes to de Vaucouleurs magnitudes to match the other mass estimates presented here. The Gallazzi et al. (2005) stellar masses (panel a) are mod-

eled in a comparable way using a similar library of star formation histories. Gallazzi et al. use a larger number of spectral absorption features in their fits; in particular, they include a number of redder features at $\sim 5000 \text{ \AA}$.

Figure 6 shows that the two spectroscopic stellar mass estimates agree very well for high- σ galaxies, with Kauffmann et al. (2003b) finding somewhat lower $M_{*, IMF}/L$ for low- σ galaxies. This may be because their measurements only use absorption lines around 4000 \AA and are therefore more strongly influenced by young subpopulations of stars than are the Gallazzi et al. estimates, resulting in underestimates of $M_{*, IMF}/L$. This difference produces a stronger slope to the $\log(M_{*, IMF}/L)$ – $\log \sigma$ relation (gray line) in Kauffmann et al. than in Gallazzi et al.

These values are compared to our single burst values in panel c, which are similar to the Kauffmann et al. values for most galaxy bins. The largest discrepancies are for galaxies with low σ and low $M_{*, IMF}/L$, where the single burst estimates are significantly lower than Kauffmann et al. These are precisely the galaxies for which we expect

¹⁴ <http://www.mpa-garching.mpg.de/SDSS/>

the single burst approximation to break down, resulting in single burst $M_{\star,IMF}/L$ values that are too low (section 4.2).

The photometry-based determinations of $M_{\star,IMF}/L$ look different from all the spectroscopic values, as shown in Figures 6d and 6e. The stellar masses shown in Figure 6d are computed using M. Blanton’s IDL code *kcorrect* v. 4.1.4 (Blanton & Roweis 2007). This code matches the SDSS *ugriz* photometry (K-corrected to $z = 0$) to a linear combination of a set of basis templates that have been determined to span the space of SDSS galaxies. The stellar masses in Figure 6e are computed using the $B - V$ galaxy colors (determined using *kcorrect*) and the conversions between galaxy color and $M_{\star,IMF}/L$ given in Table 7 of Bell et al. (2003). The Bell et al. conversions are based on fits of the full *ugrizK* combined SDSS and 2MASS photometry for SDSS Early Data Release (Stoughton et al. 2002) galaxies to a set of models spanning a range of star formation histories. In both cases, the colors are computed from photometry that has been matched to the SDSS 3’’ spectral fiber aperture in order to provide consistency with the spectroscopically-derived values of $M_{\star,IMF}/L$ (see appendix B). These photometrically-derived values of $M_{\star,IMF}/L$ show much weaker variation with σ and much smaller spread at fixed σ than the spectroscopically-derived values.

The increased spread in the spectroscopic values can be understood from Figure 4b. As discussed in section 4.1, the lines of constant $g - r$ in the models of Figure 4b run very nearly parallel to the lines of constant σ in the data. The spectroscopic data are thus capable of differentiating between different star formation histories and different $M_{\star,IMF}/L$ values at fixed σ , which the photometry-based values cannot do.

Throughout the rest of this analysis, we will use the Gallazzi et al. (2005) values for $M_{\star,IMF}/L$ because they capture the variation in $M_{\star,IMF}/L$ at fixed σ (unlike the photometry-based measurements) but are likely to be less biased toward younger sub-populations than the Kauffmann et al. (2003b) and especially the single burst values.

4.4. M_{dyn}/L versus $M_{\star,IMF}/L$

As a final point of comparison, Figure 6f shows M_{dyn}/L as a function of σ . It is clear that none of the $M_{\star,IMF}/L$ measurements (panels a–e) resemble M_{dyn}/L . *No matter which method is used to measure $M_{\star,IMF}/L$, stellar population effects cannot reproduce the observed variation in M_{dyn}/L .*

In the first place, none of the $M_{\star,IMF}/L$ measurements have a slope with σ that is as steep as the slope of the observed M_{dyn}/L - σ relation. This means that stellar population effects are not enough to explain the tilt of the FP, as has been demonstrated by numerous previous authors (e.g., Pahre et al. 1995; Prugniel & Simien 1996; Pahre et al. 1998; Scodreggio et al. 1998; Mobasher et al. 1999; Padmanabhan et al. 2004; Trujillo et al. 2004; Jun & Im 2008; La Barbera et al. 2008; Hyde & Bernardi 2009).¹⁵

¹⁵ In contrast to our results and other previous studies, Allanson et al. (2009) find that the assumption of single burst star formation histories predicts a strong enough scaling of $M_{\star,IMF}/L$ with σ to account for the entire σ tilt of the FP. While our re-

In the second place, it is clear from Figure 6 that $M_{\star,IMF}/L$ variations cannot provide enough spread at fixed σ to match the observed variation in M_{dyn}/L . *This new result indicates that stellar populations contribute little to the thickness of the FP*, despite the fact that residuals from the FP appear to be correlated with stellar population properties (Forbes et al. 1998; Wuyts et al. 2004; Gargiulo et al. 2009, Paper II). This is because the stellar population differences through the thickness of the FP show an *anti*-correlation between age and [Fe/H]. This anti-correlation, while not exactly parallel to lines of constant $M_{\star,IMF}/L$ (see Figure 4), is in a similar direction and therefore limits the differences in $M_{\star,IMF}/L$ that result from the stellar population differences at fixed σ .

The marked difference of Figure 6f from Figure 6a–e requires that there be variations in M_{dyn}/M_{\star} (the dark matter fraction) and/or in $M_{\star}/M_{\star,IMF}$ (the IMF) among quiescent galaxies. At least one of these quantities must vary *along* the FP to reproduce the observed σ tilt of the plane. One or both of them must also vary *through the thickness* of the FP. Furthermore, these variations likely dominate over stellar population variations both along and through the FP.

5. MASS-TO-LIGHT RATIOS IN 3D FP SPACE

Having quantified the variation of $M_{\star,IMF}/L$ for our sample galaxies, as well as the systematic uncertainties in $M_{\star,IMF}/L$ measurements, we can now examine how the stellar population term contributes to the total observed variation of M_{dyn}/L throughout 3D FP space. In essence, we will be *dividing out* the variations due to stellar populations and thereby mapping how the remaining term ($M_{dyn}/M_{\star,IMF}$) varies over the plane and through it.

Section 5.1 focuses on the FP midplane, examining how $M_{\star,IMF}/L$ and $M_{dyn}/M_{\star,IMF}$ contribute separately to the tilt of the FP. We show that, not only does the tilt of the FP require contributions from both $M_{\star,IMF}/L$ and $M_{dyn}/M_{\star,IMF}$, but that these two components of the tilt rotate the plane *around different axes* in the 3D parameter space. Section 5.2 then maps both these quantities in a cross-section through the FP, examining how each contributes to the thickness of the FP. We show that the thickness of the FP is dominated by variations in $M_{dyn}/M_{\star,IMF}$, with $M_{\star,IMF}/L$ contributing only $\sim 22\%$ of the variation. Finally, section 5.3 distills the quantitative results of this analysis by presenting fitting functions for the total mass-to-light variation (M_{dyn}/L_V), the stellar population contribution ($M_{\star,IMF}/L$), the dark matter/IMF contribution ($M_{dyn}/M_{\star,IMF}$), and the associated surface mass density of stars ($\Sigma_{\star,IMF}$) as functions of the three FP variables: σ , R_e , and ΔI_e .

5.1. The Tilt of the FP in 3D

sults agree that single burst models produce substantially steeper slopes than those computed with more complex star formation histories, we find that even single burst models cannot produce the entire σ tilt of the plane. A comparison between our Figure 6 and their Figure 12 suggests that this difference is due to differences in the slope of the observed M_{dyn}/L - σ relation (they find $M_{dyn}/L \propto \sigma^{0.79}$ while we find $M_{dyn}/L \propto \sigma^{0.95 \pm 0.04}$). Our single burst stellar population modelling results agree with theirs; they find $M_{\star,IMF}/L \propto \sigma^{0.66}$ for a single burst model, while we find $M_{\star,IMF}/L \propto \sigma^{0.67 \pm 0.04}$.

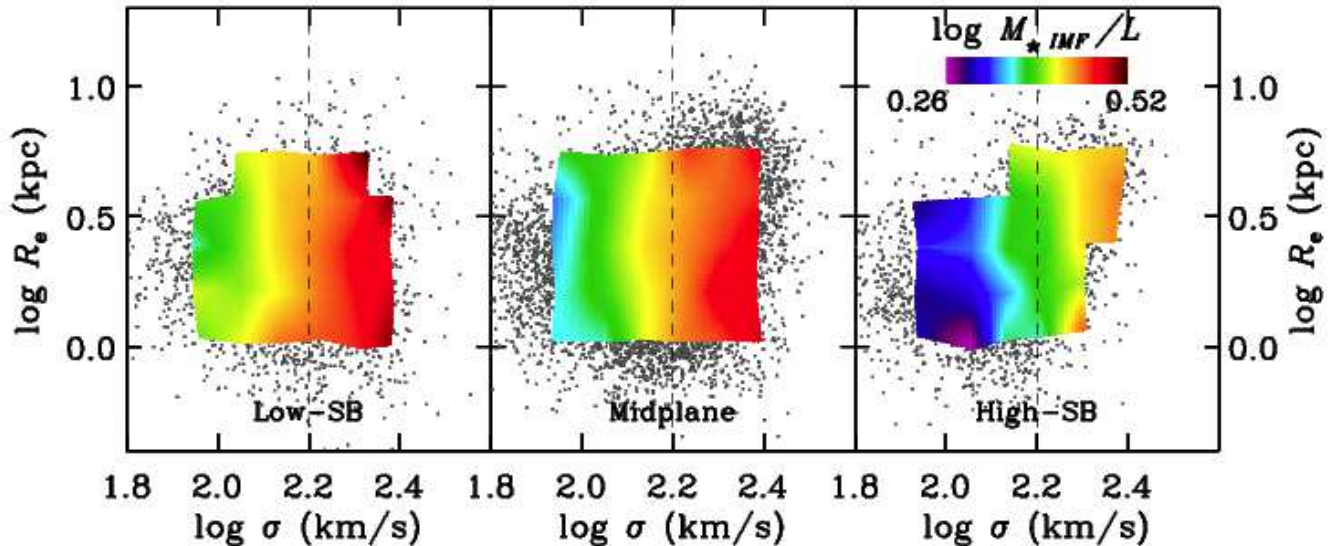


Figure 7. The FP tilt contribution from stellar population effects, mapped throughout 3D FP space. Data points in each panel represent the sample galaxies divided into three slices in surface brightness, as in Figure 1. The overlaid color contours show variations in $M_{*,IMF}/L$ in this space, measured using the values of Gallazzi et al. (2005). On the FP midplane (center panel), lines of constant $M_{*,IMF}/L$ follow lines of constant σ (dashed line); $M_{*,IMF}/L$ is independent of R_e . This indicates that $M_{*,IMF}/L$ is a function of only σ ($M_{*,IMF}/L = f(\sigma)$) on the FP. The low- and high-surface-brightness slices show the same effect, with lines of constant $M_{*,IMF}/L$ running vertically. However, they show zeropoint shifts from the midplane, with the low- and high-surface-brightness galaxies have systematically higher and lower $M_{*,IMF}/L$, respectively. These trends in $M_{*,IMF}/L$ are as predicted from the stellar population maps in Paper II.

Figure 7 maps how the stellar population $M_{*,IMF}/L$ component varies over the FP using the bins presented in Figure 1. The three panels show the three slices in surface brightness, including the midplane and the slices above and below the plane. The overlaid contours indicate the median $M_{*,IMF}/L$ values for each bin in FP space, using the Gallazzi et al. (2005) measurements. The contours are constructed by plotting the median value of $M_{*,IMF}/L$ for each bin at the point corresponding to the median values of σ and R_e for the bin. The values of $M_{*,IMF}/L$ are then linearly interpolated between the 6×5 grid of bins in each surface brightness slice to produce a continuous map of $M_{*,IMF}/L$ along each slice.

Looking first at the FP midplane (center panel), it is clear that $M_{*,IMF}/L$ depends on σ but is independent of R_e . Lines of constant $M_{*,IMF}/L$ follow lines of constant σ (dashed line). Therefore, we find that $M_{*,IMF}/L$ is a function only of σ on the FP. This is expected from Paper II, where we showed that all stellar population properties (age, [Fe/H], [Mg/H], and [Mg/Fe]) follow lines of constant σ on the FP and are essentially independent of R_e . It therefore follows that the known stellar population contribution to M_{dyn}/L should also follow lines of constant σ .

The low- and high-surface-brightness panels above and below the midplane show the same behavior: $M_{*,IMF}/L$ again follows lines of constant σ and is independent of R_e . However, the zeropoint of the relation shifts such that galaxies in the low-surface-brightness slice have *higher* $M_{*,IMF}/L$ for a given σ than their counterparts on the FP midplane. Similarly, galaxies in the high-surface-brightness slice have *lower* $M_{*,IMF}/L$ for a given σ . This demonstrates that there are $M_{*,IMF}/L$ variations through the *thickness* of the FP as well, although they are relatively weak. We will study these variations through

the thickness of the FP in more detail in §5.2.

With $M_{*,IMF}/L$ now mapped, we can divide it out to isolate the map of $M_{dyn}/M_{*,IMF}$ alone. We do this by calculating the ratio of the two known quantities M_{dyn}/L and $M_{*,IMF}/L$. The resultant map, which shows the dark matter/IMF contribution $M_{dyn}/M_{*,IMF}$, is shown in Figure 8.¹⁶ The data and contours are constructed in the same way as Figure 7.

A major result of this paper is illustrated in Figure 8: lines of constant $M_{dyn}/M_{*,IMF}$ on the FP midplane (center panel) follow a noticeably different slope than the lines of constant $M_{*,IMF}/L$ in Figure 7. The new lines run approximately parallel to lines of constant M_{dyn} (dashed line, with $M_{dyn} \propto \sigma^2 R_e$), indicating that on the FP midplane $M_{dyn}/M_{*,IMF}$ is a function of M_{dyn} . Similar behavior is seen in the low- and high-surface-brightness panels. Both Gallazzi et al. (2005) and Hyde & Bernardi (2009) showed a correlation between $M_{*,IMF}$ and M_{dyn} that was strong, but this is the first time that it has been shown to be the *best* correlation, by mapping $M_{dyn}/M_{*,IMF}$ explicitly in 3D FP space.

By examining the two contributions to the FP tilt in 3D space, we have revealed that *the two suspected causes of*

¹⁶ The values of $M_{dyn}/M_{*,IMF}$ run from -0.13 to $+0.50$. Negative values of $M_{dyn}/M_{*,IMF}$ are clearly nonsensical if $M_{dyn} = 5\sigma^2 R_e/G$ gives a true representation of the total mass and the Chabrier IMF is a good approximation to the true IMF in these galaxies; a galaxy cannot contain less total mass than its stellar mass. However, modest changes to the assumed IMF (e.g., Longhetti & Saracco 2009) or to the constant used to compute M_{dyn} will produce zeropoint shifts of the needed magnitude (~ 0.1 dex). In this work, we have focused on trends through FP space, for which the zeropoint is not relevant, rather than on absolute measurements of $M_{*,IMF}/L$. It is worth noting however that, as computed here, the single burst values of $M_{*,IMF}/L$ are the only ones for which all galaxy bins give $M_{*,IMF} \leq M_{dyn}$.

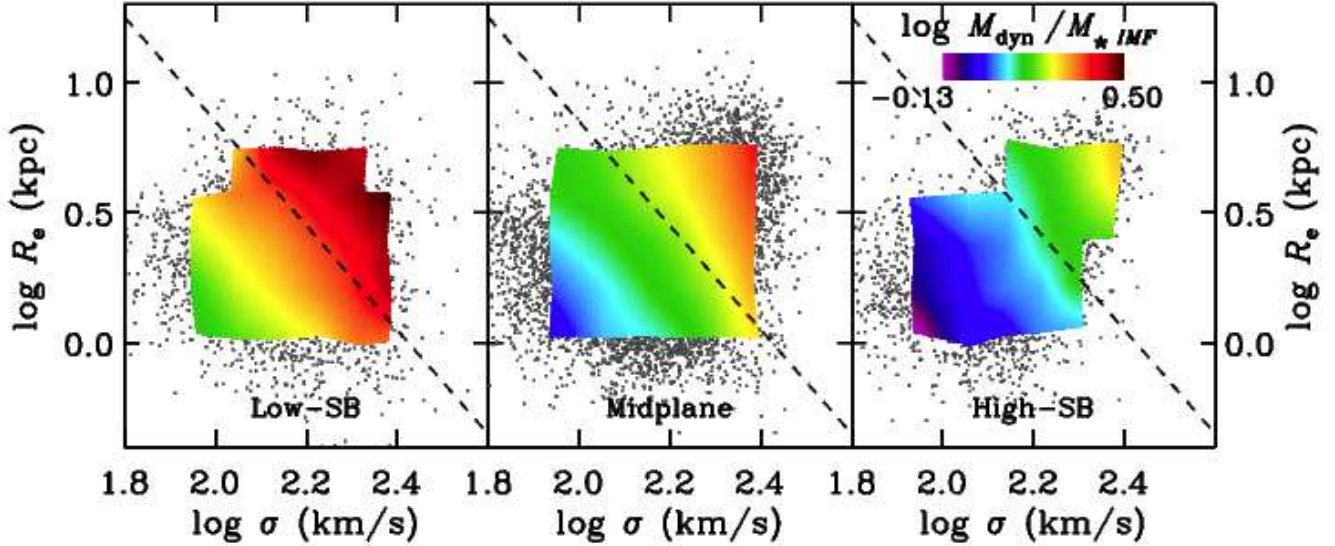


Figure 8. The FP tilt contribution from varying dark matter/IMF effects, mapped throughout 3D FP space. Data points in each panel represent the sample galaxies, divided into three slices in surface brightness, as in Figure 1. The overlaid color contours show variations in $M_{dyn}/M_{*,IMF}$ in this space. On the FP midplane (center panel), lines of constant $M_{dyn}/M_{*,IMF}$ approximately follow lines of constant M_{dyn} (dashed line) such that $M_{dyn}/M_{*,IMF} = f(M_{dyn})$ on the FP. The two components of the FP tilt therefore rotate the plane around different axes. The low-surface-brightness (high-surface-brightness) slice shows the same effect, but with a zeropoint shift such that $M_{dyn}/M_{*,IMF}$ values are higher (lower) than the midplane values.

FP tilt rotate the plane around different axes. The stellar population contribution has $M_{*,IMF}/L \approx f(\sigma)$, while the dark matter/IMF contribution has $M_{dyn}/M_{*,IMF} \approx g(M_{dyn}) = g(\sigma^2 R_e)$. This indicates that the tilt of the FP cannot be parameterized as a simple power-law function of M_{dyn} or M_* or L or σ . Instead, it takes the functional form $f(\sigma) \times g(M_{dyn})$.

Figure 8 also illustrates a second major result of this paper. Lines of constant $M_{dyn}/M_{*,IMF}$ run parallel to lines of constant M_{dyn} in all three panels, but there is a zeropoint shift between the slices. The low-surface-brightness and high-surface-brightness slices have respectively higher and lower values of $M_{dyn}/M_{*,IMF}$ for a given σ than do their counterparts on the FP midplane. The sign is the same as the shift of $M_{*,IMF}/L$ seen in the three panels of Figure 7. Both 3D maps reveal that the stellar population effects and the dark matter fraction/IMF effects which contribute to the FP tilt contribute also to the thickness of the FP as well. Section 5.2 explores this second trend in more detail.

Focusing for the time being on the FP midplane alone, we quantify the contributions of the two tilt components in Figure 9. The left panels show the stellar population (upper left) and dark matter/IMF (lower left) contributions to the σ tilt of the FP. Only the galaxy bins on the FP midplane slice are included. $M_{*,IMF}/L$ is a very tight function of σ . To quantify the stellar population contribution to the σ tilt of the FP, we calculate the ratio $\Delta \log(M_{*,IMF}/L)/\Delta \log \sigma$. This is the first of several such ratios we will discuss; hereafter we refer to them as “ Δ - Δ ” relations. Note that the numeric value of $\Delta \log(M_{*,IMF}/L)/\Delta \log \sigma$ is equivalent to the quantity μ in the relation $M_{*,IMF}/L \propto \sigma^\mu$. A linear least-squares fit, weighted by the number of galaxies in each bin, gives $M_{*,IMF}/L \propto \sigma^{0.30}$ and scatter of only 0.01 dex. Meanwhile, $M_{dyn}/M_{*,IMF}$ is a less tight function of σ , with $M_{dyn}/M_{*,IMF} \propto \sigma^{0.65}$ and scatter of 0.05 dex.

Comparing the two slopes shows that *dark matter/IMF variations contribute twice as much to the σ tilt of the FP as do stellar population variations.*

We can instead choose to parameterize the FP tilt as a function of M_{dyn} (i.e., the “total tilt” of the FP). In this case, the Δ - Δ relation between $M_{dyn}/M_{*,IMF}$ and M_{dyn} (lower right panel) is significantly tighter than that between $M_{dyn}/M_{*,IMF}$ and σ (lower left panel), with $M_{dyn}/M_{*,IMF} \propto M_{dyn}^{0.24}$ and scatter of only 0.02 dex. In contrast, $M_{*,IMF}/L$ shows a less tight relation with M_{dyn} (upper right panel), giving $M_{*,IMF}/L \propto M_{dyn}^{0.08}$ and scatter of 0.03 dex. Comparing the slopes of the two relations shows that *dark matter/IMF variations contribute three times as much to the total tilt of the FP as do stellar population variations.*

Figures 7–9 use the Gallazzi et al. (2005) values of $M_{*,IMF}/L$, but any other choice gives qualitatively similar results: in the FP midplane, lines of constant $M_{*,IMF}/L$ follow lines of constant σ , while lines of constant $M_{dyn}/M_{*,IMF}$ follow lines of constant M_{dyn} . However, *quantifying* the various Δ - Δ relations depends on the choice of $M_{*,IMF}/L$.

These differences are summarized in Table 1. The top section of the table shows the stellar population and dark matter/IMF contributions to the σ tilt of the FP, measured using the five different estimates of $M_{*,IMF}/L$ that were discussed in §4.3. The Gallazzi et al. (2005) values are those illustrated in the left panels of Figure 9; values using other $M_{*,IMF}/L$ estimates are computed in the same way. Notice that, depending on the chosen method for estimating $M_{*,IMF}/L$, the stellar population contribution to the σ tilt of the FP ranges from 13–70%, with our preferred value falling in the middle of the range at 32%.

The middle section of Table 1 quantifies the stellar population and dark matter/IMF contributions to the

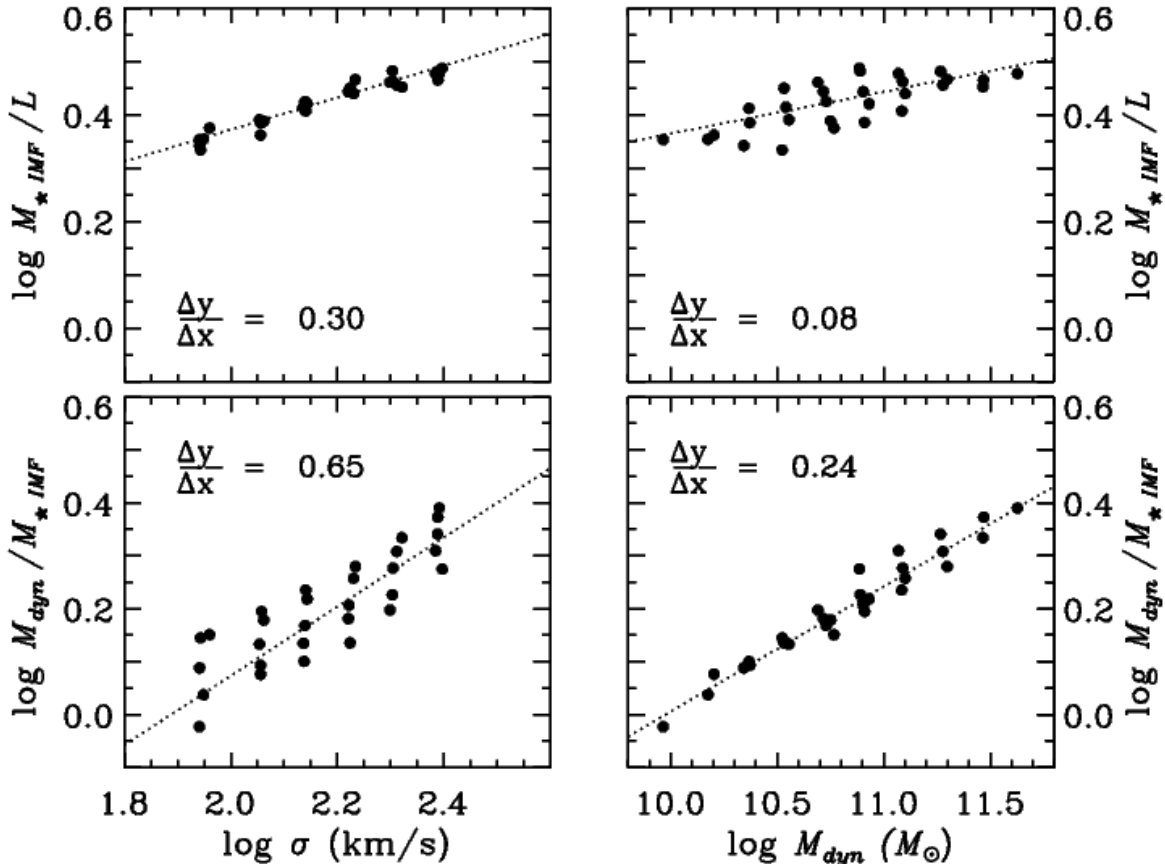


Figure 9. The two tilts of the Fundamental Plane. Only galaxy bins from the FP midplane are shown. *Left:* The stellar population (upper panel) and dark matter/IMF (bottom panel) contributions to the σ tilt of the FP. The stellar population component is a tight function of σ , with $M_{\star,IMF}/L \propto \sigma^{0.30}$ and scatter of 0.01 dex. The dark matter/IMF component shows more scatter when plotted against σ , with $M_{dyn}/M_{\star,IMF} \propto \sigma^{0.65}$ and scatter of 0.05 dex. Comparing the slopes of the two relations indicates that dark matter/IMF effects contribute 2/3 of the σ tilt on the FP. *Right:* The stellar population (upper panel) and dark matter/IMF (lower panel) contributions to the total tilt of the FP. Here, the tightness of the relations is the opposite way round: the stellar population term shows 0.03 dex of scatter at fixed M_{dyn} with $M_{\star,IMF}/L \propto M_{dyn}^{0.08}$, while the dark matter/IMF term shows only 0.02 dex of scatter and has $M_{dyn}/M_{\star,IMF} \propto M_{dyn}^{0.24}$. Dark matter/IMF effects contribute 3/4 of the total tilt of the FP.

total tilt of the FP, based on the five different estimates of $M_{\star,IMF}/L$. For any given estimate, stellar populations contribute less to the total tilt of the FP than they do to the σ tilt, ranging from 13–58%, with our preferred value falling in the middle at 25%.

For both the σ tilt and the total tilt, using the single burst values gives the strongest variations in $M_{\star,IMF}/L$. This is due to the fact that single burst models likely underestimate $M_{\star,IMF}/L$ for galaxies with the lowest values of $M_{\star,IMF}/L$, making the trend look stronger than it actually is (see section 4.2). In contrast, the photometry-based determinations of $M_{\star,IMF}/L$ from Blanton & Roweis (2007) and Bell et al. (2003) produce very little variation in $M_{\star,IMF}/L$ —all galaxy bins have nearly identical values—so that stellar population effects contribute very little to the σ tilt or total tilt using these estimates.

The key point is that, regardless of which method is used to estimate $M_{\star,IMF}/L$, both stellar population and dark matter/IMF effects are *required* to explain the tilt of the FP. Furthermore, these two components of the FP tilt rotate the plane around different axes.

Recently, Treu et al. (2010) have argued using entirely

independent methods that $M_{dyn}/M_{\star,IMF}$ (which they parameterize as an “IMF mismatch parameter” α) varies as a function of σ , such that higher- σ galaxies have higher α . They find $\log(M_{dyn}/M_{\star,IMF}) \propto (1.20 \pm 0.25) \log \sigma$ and argue that these variations are either due to differences in the IMF as a function of σ , or differences in the central profile of the host dark matter halo. The slope of the trend they find is somewhat larger than what is presented here; their values of $M_{\star,IMF}$ are inferred from multiband photometry and are thus best compared to the Blanton et al. or Bell et al. values derived here in Table 1, which give $\log(M_{dyn}/M_{\star,IMF}) \propto 0.83 \log \sigma$ and $\log(M_{dyn}/M_{\star,IMF}) \propto 0.73 \log \sigma$, respectively.

5.2. The Thickness of the FP

Having discussed the tilt of the FP in detail by examining trends along the FP midplane, we now switch over to examining trends through the thickness of the FP. Figures 7 and 8 showed that the high- and low-SB slices above and below the FP midplane exhibited the same quantitative trends as the midplane, but with zeropoint shifts in both $M_{\star,IMF}/L$ and $M_{dyn}/M_{\star,IMF}$. In this section, we present a detailed exploration of the trends in

Table 1
Stellar Population Contribution to the “ σ Tilt”, Total Tilt, and the Thickness of the FP
for Various Methods of Measuring $M_{\star,IMF}$

	Gallazzi [*]	Kauffmann [†]	Single Burst [‡]	Blanton [§]	Bell [¶]
The σ Tilt of the FP					
$\frac{\Delta \log(M_{\star,IMF}/L)}{\Delta \log \sigma}$	0.30	0.45	0.67	0.12	0.22
$\frac{\Delta \log(M_{dyn}/M_{\star,IMF})}{\Delta \log \sigma}$	0.65	0.50	0.29	0.83	0.73
Fraction from Stellar Pops	32%	47%	70%	13%	23%
The Total (M_{dyn}) Tilt of the FP					
$\frac{\Delta \log(M_{\star,IMF}/L)}{\Delta \log M_{dyn}}$	0.08	0.13	0.18	0.04	0.07
$\frac{\Delta \log(M_{dyn}/M_{\star,IMF})}{\Delta \log M_{dyn}}$	0.24	0.19	0.13	0.28	0.25
Fraction from Stellar Pops	25%	41%	58%	13%	22%
The Thickness of the FP					
$\frac{\Delta \log(M_{\star,IMF}/L)}{\Delta \log I_e}$	-0.22	-0.20	-0.54	-0.02	-0.02
$\frac{\Delta \log(M_{dyn}/M_{\star,IMF})}{\Delta \log I_e}$	-0.79	-0.81	-0.48	-1.00	-0.99
Fraction from Stellar Pops	22%	20%	53%	2%	2%

Note. —

^{*}Values computed using the Gallazzi et al. (2005) measurements of $M_{\star,IMF}$. These are our preferred values, as discussed in section 4.3.

[†]Values computed using the Kauffmann et al. (2003b) measurements of $M_{\star,IMF}$.

[‡]Values computed using the single burst measurements of $M_{\star,IMF}$ from section 4.1.

[§]Values computed using the Blanton & Roweis (2007) measurements of $M_{\star,IMF}$.

[¶]Values computed using the Bell et al. (2003) measurements of $M_{\star,IMF}$.

both quantities through the thickness of the plane.

To illustrate this, we adopt the binning strategy illustrated in Figure 2, where bins are now defined in a 2D cross-section through the FP. Figure 10 maps $M_{\star,IMF}/L$ and $M_{dyn}/M_{\star,IMF}$ across the FP cross-section. The same color scale is used in both panels to facilitate comparison. $M_{\star,IMF}/L$ and $M_{dyn}/M_{\star,IMF}$ behave similarly in this projection; both have maximum values among high- σ , low- I_e galaxies and minimum values at low σ and high I_e . Lines of constant values run diagonally from upper right to lower left. The main difference between these two parameters is the range of variation. The range of $M_{\star,IMF}/L$ values is *much smaller* than the range covered by $M_{dyn}/M_{\star,IMF}$, particularly in the ΔI_e dimension.¹⁷

We have already quantified changes in $M_{\star,IMF}/L$ and

$M_{dyn}/M_{\star,IMF}$ along the plane in Figure 9. Figure 11 makes a similar comparison for the variations through the thickness of the plane. To focus on the trends *through* the plane, we normalize out any trends *along* the plane by subtracting mid-plane values of $M_{\star,IMF}/L$ and $M_{dyn}/M_{\star,IMF}$ at each bin in (σ, R_e) . The various (σ, R_e) bins are represented by gray lines. The thick black lines show fits to the ensemble of data values, with slopes as indicated. Comparing these slopes shows that $M_{dyn}/M_{\star,IMF}$ varies more than three times as much through the thickness of the FP as does $M_{\star,IMF}/L$. Dark matter and/or IMF variations therefore provide the dominant contribution to the thickness of the FP.

As with the FP tilt, the relative contributions of the stellar population and dark matter/IMF terms depends on which estimates of $M_{\star,IMF}/L$ are used. These quantitative differences are summarized in the bottom sec-

¹⁷ This projection of the FP averages over R_e . Figures 7–8 showed that, while $M_{\star,IMF}/L$ is independent of R_e , $M_{dyn}/M_{\star,IMF}$ is not. Thus the $M_{dyn}/M_{\star,IMF}$ values mapped in Figure 10 average over a range of $M_{dyn}/M_{\star,IMF}$ values at each point in the FP cross-section and are presented for illustrative purposes only. We have dealt with this variation in all quantitative

presentations of the $M_{dyn}/M_{\star,IMF}$ - $\log I_e$ Δ - Δ relations (Table 1 and Figure 11) by explicitly subtracting off the dependence of $M_{dyn}/M_{\star,IMF}$ on R_e .

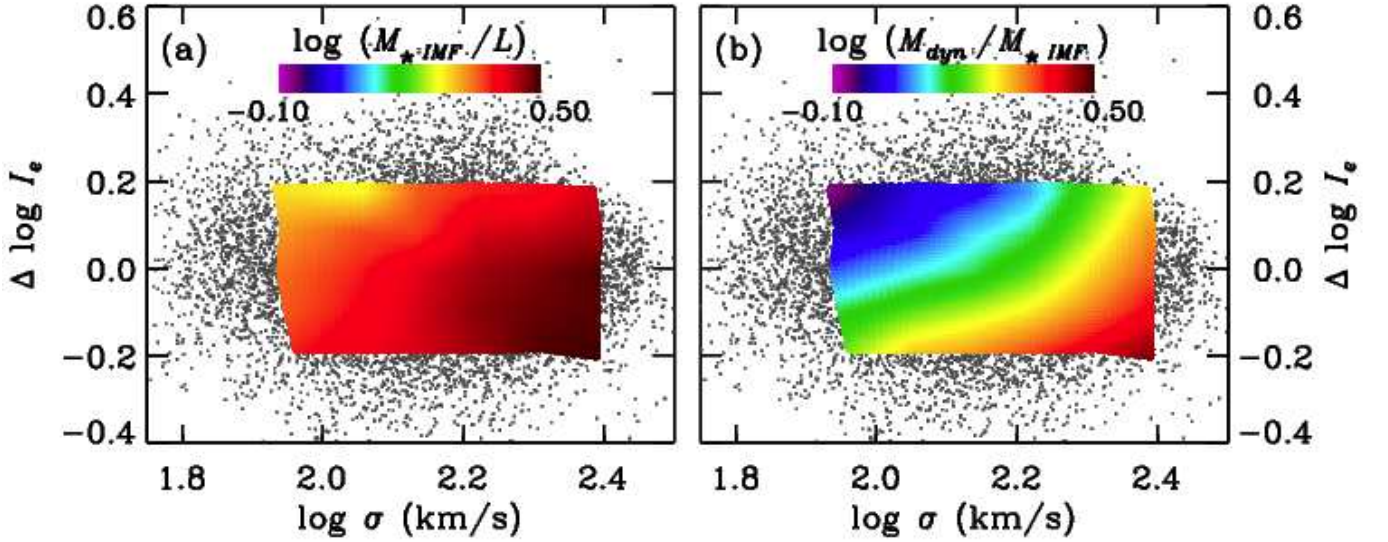


Figure 10. The contribution of (a) stellar population variations and (b) variable dark matter/IMF to the *thickness* of the FP. Individual galaxies are plotted as points in ΔI_e - σ space, as in Figure 2. Color contours indicate $M_{*,IMF}/L$ and $M_{dyn}/M_{*,IMF}$ and are constructed in the same way as Figures 7–8. The color maps in (a) and (b) are shown on the same scale. Both $M_{*,IMF}/L$ and $M_{dyn}/M_{*,IMF}$ vary through the thickness of the FP with ΔI_e . The variation in $M_{dyn}/M_{*,IMF}$ is much stronger than the variation in $M_{*,IMF}/L$ and therefore dominates the thickness of the FP.

tion of Table 1. Using the Gallazzi et al. (2005) measurements of $M_{*,IMF}/L$, stellar population effects contribute only 22% of the tilt of the FP—the remaining 78% must be due to dark matter and/or IMF variations. The Kauffmann et al. (2003b) measurements give similar results. As we saw with the FP tilt, using single burst models to measure $M_{*,IMF}/L$ through the thickness of the FP results in a larger contribution from stellar population effects (53%) because low values of $M_{*,IMF}/L$ are underestimated, while the photometry-based measurements lead to very small contributions from stellar population effects (2%) because of the age-metallicity degeneracy. Considering the full range of models for $M_{*,IMF}/L$, stellar populations contribute 2–53% of the thickness of the FP, which means that dark matter/IMF effects contribute 47–98%.

From Table 1 it is clear that, regardless of which method is used to determine $M_{*,IMF}$, variations in the IMF and/or the inner dark matter fraction in galaxies are required to explain *both* the tilt and the thickness of the FP. They contribute at least 1/2–1/3 of each effect, and it is likely that they dominate both.

This leads to an important point. To the extent that $M_{*,IMF}/L$ variations through the thickness of the FP can be ignored (since they constitute only 22% of the total variation using the Gallazzi et al. 2005 models), the change in I_e through the plane must be due to changes in $M_{dyn}/M_{*,IMF}$. However, at a fixed point in σ and R_e , M_{dyn} is constant by definition. Thus changes in $M_{dyn}/M_{*,IMF}$ through the plane are primarily due to changes in $M_{*,IMF}$ within R_e , which means that *stellar mass surface density* ($\Sigma_{*,IMF}$) is changing. In other words, the low surface brightnesses of galaxies below the plane are due to low stellar mass surface densities, not to the fact that their stellar populations are dim. Galaxies do not move below the plane by fading; they were built that way.

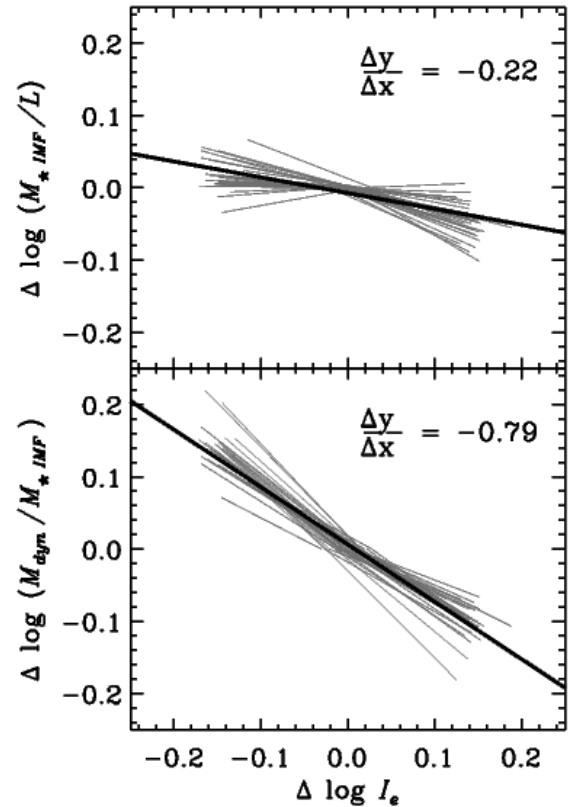


Figure 11. *Top:* The change in $M_{*,IMF}/L$ through the thickness of the FP. The gray lines represent different bins in (σ, R_e) , with the $M_{*,IMF}/L$ value of the midplane bin subtracted off. $M_{*,IMF}/L$ decreases by 0.22 dex for every 1 dex increase in ΔI_e . *Bottom:* The change in $M_{dyn}/M_{*,IMF}$ through the thickness of the FP. Colors and normalization are as in the top panel. $M_{dyn}/M_{*,IMF}$ decreases by 0.79 dex for every 1 dex increase in ΔI_e . $M_{dyn}/M_{*,IMF}$ therefore varies more than three times as much as $M_{*,IMF}/L$ through the thickness of the FP.

Table 2
Fitting Formulas for Mass-to-Light Ratio Contributions

As Functions of σ , R_e , and ΔI_e *										
$\log (M_{dyn}/L_V)$	=	0.85 (0.01)	$\log \sigma'$	+	0.22 (0.01)	$\log R'_e$	-	1.04 (0.01)	$\Delta \log I_e$	+ 0.62 (0.01)
$\log (M_{dyn}/M_{*,IMF})$	=	0.53 (0.02)	$\log \sigma'$	+	0.22 (0.01)	$\log R'_e$	-	0.80 (0.02)	$\Delta \log I_e$	+ 0.20 (0.01)
$\log (M_{*,IMF}/L_V)$	=	0.31 (0.01)	$\log \sigma'$	+	0.003 (0.01)	$\log R'_e$	-	0.24 (0.02)	$\Delta \log I_e$	+ 0.42 (0.01)
$\log (\Sigma_{*,IMF})$	=	1.49 (0.01)	$\log \sigma'$	-	1.20 (0.01)	$\log R'_e$	+	0.80 (0.02)	$\Delta \log I_e$	+ 3.81 (0.01)
As Functions of σ , R_e , and I_e										
$\log (M_{dyn}/L_V)$	=	2.00 (0.01)	$\log \sigma'$	-	0.97 (0.01)	$\log R'_e$	-	0.95 (0.01)	$\log I'_e$	+ 0.61 (0.01)
$\log (M_{dyn}/M_{*,IMF})$	=	1.43 (0.03)	$\log \sigma'$	-	0.71 (0.03)	$\log R'_e$	-	0.74 (0.02)	$\log I'_e$	+ 0.20 (0.01)
$\log (M_{*,IMF}/L_V)$	=	0.57 (0.03)	$\log \sigma'$	-	0.27 (0.02)	$\log R'_e$	-	0.22 (0.02)	$\log I'_e$	+ 0.42 (0.03)
$\log (\Sigma_{*,IMF})$	=	0.60 (0.02)	$\log \sigma'$	-	0.27 (0.02)	$\log R'_e$	+	0.74 (0.02)	$\log I'_e$	+ 3.82 (0.01)

Note. — $\sigma' \equiv \sigma/150 \text{ km s}^{-1}$, $R'_e \equiv R_e/2.5 \text{ kpc}$, and $I'_e \equiv I_e/400L_\odot \text{ pc}^{-2}$.
* $\Delta \log I_e$ is defined as $\Delta \log I_e = \log I_e - (1.16 \log \sigma - 1.21 \log R_e + 0.55)$ (see Figure 1).

5.3. Fitting Formulas for Mass-to-Light Ratios as Functions of σ , R_e , and ΔI_e

In this analysis, we have quantified the variations of M_{dyn}/L , $M_{dyn}/M_{*,IMF}$, and $M_{*,IMF}/L$ throughout 3D FP space. These results can be summarized by fitting each of these parameters as a function of σ , R_e , and ΔI_e . We assume that each mass parameter is a first-order function of $\log \sigma$, $\log R_e$, and $\Delta \log I_e$, then use the IDL package *mpfit.pro* (Markwardt 2009) implementation of Levenberg-Marquardt minimization to find the best such solution. Note that because σ , R_e , and ΔI_e are not orthogonal coordinates, the exponents derived from explicitly 3D fitting do not in general exactly match those presented from 1D fits in sections 5.1–5.2. The correct quantification of the dependence on each FP parameter must be derived from explicitly 3D fits.

The resulting functional forms are given in the top half of Table 2, using the Gallazzi et al. (2005) values for $M_{*,IMF}/L$. Values in parentheses under each function give the 1σ error in each parameter of the fit, computed from the covariance matrix of the fit. We also include fits to the effective stellar mass surface density, defined as $\Sigma_{*,IMF} = M_{*,IMF}/(2\pi R_e^2)$ in analogy with the effective surface brightness. The parameters of the $M_{*,IMF}/L$ fit in Table 2 show that $M_{*,IMF}/L$ is independent of R_e , as discussed in section 5.1. For completeness, in the bottom section of the table we also include fits as explicit functions of $\log I_e$, rather than using the ΔI_e parameterization.

Figure 12 illustrates the quality of these fits. In each panel, we plot the median value of M_{dyn}/L , $M_{dyn}/M_{*,IMF}$, $M_{*,IMF}/L$, or $\Sigma_{*,IMF}$ as measured for each bin against the value predicted by the fits in Table 2. Panels a–c are plotted on the same scale to facili-

tate comparison. The standard deviation of the scatter about the one-to-one relation is indicated in each panel. The fits do an excellent job of reproducing the median observed values, with scatter $\leq 0.02 \text{ dex}$ (i.e., $\leq 5\%$) in all cases. The relations can therefore be used to estimate values of $M_{dyn}/M_{*,IMF}$, $M_{*,IMF}/L$, and $\Sigma_{*,IMF}$ for ensembles of SDSS galaxies from the parameters $\langle \sigma \rangle$, $\langle R_e \rangle$, and $\langle I_e \rangle$. Note that these values are correct in the statistical sense only, as the galaxy-to-galaxy variation in stellar population properties within a bin cannot be estimated from the stacking analysis presented here.

6. COUPLED DARK MATTER/IMF VARIATIONS AND STAR FORMATION HISTORIES THROUGH THE THICKNESS OF THE FUNDAMENTAL PLANE

We have examined in detail the mass-to-light ratios of our sample of $\sim 16,000$ quiescent galaxies from the SDSS. We have identified and quantified the contribution of stellar population effects ($M_{*,IMF}/L$) both along the FP and through its thickness. By comparing these modest variations with the much larger observed variation in M_{dyn}/L , we have argued for substantial additional variations in $M_{dyn}/M_{*,IMF}$ due to variations in the IMF or in the inner dark matter fractions in some galaxies. In this discussion, we combine this information with the stellar population results of Paper II to evaluate three possible physical mechanisms behind the observed $M_{dyn}/M_{*,IMF}$ variation, with particular focus on variations *through the thickness* of the FP.

For reference, the correlations between the structural properties of galaxies, their mass ratios, and their stellar population properties are summarized in Table 3. This table combines the results of this work and those of Paper II. For each of the stellar population properties derived in Paper II—age, [Fe/H], [Mg/H], and [Mg/Fe]—

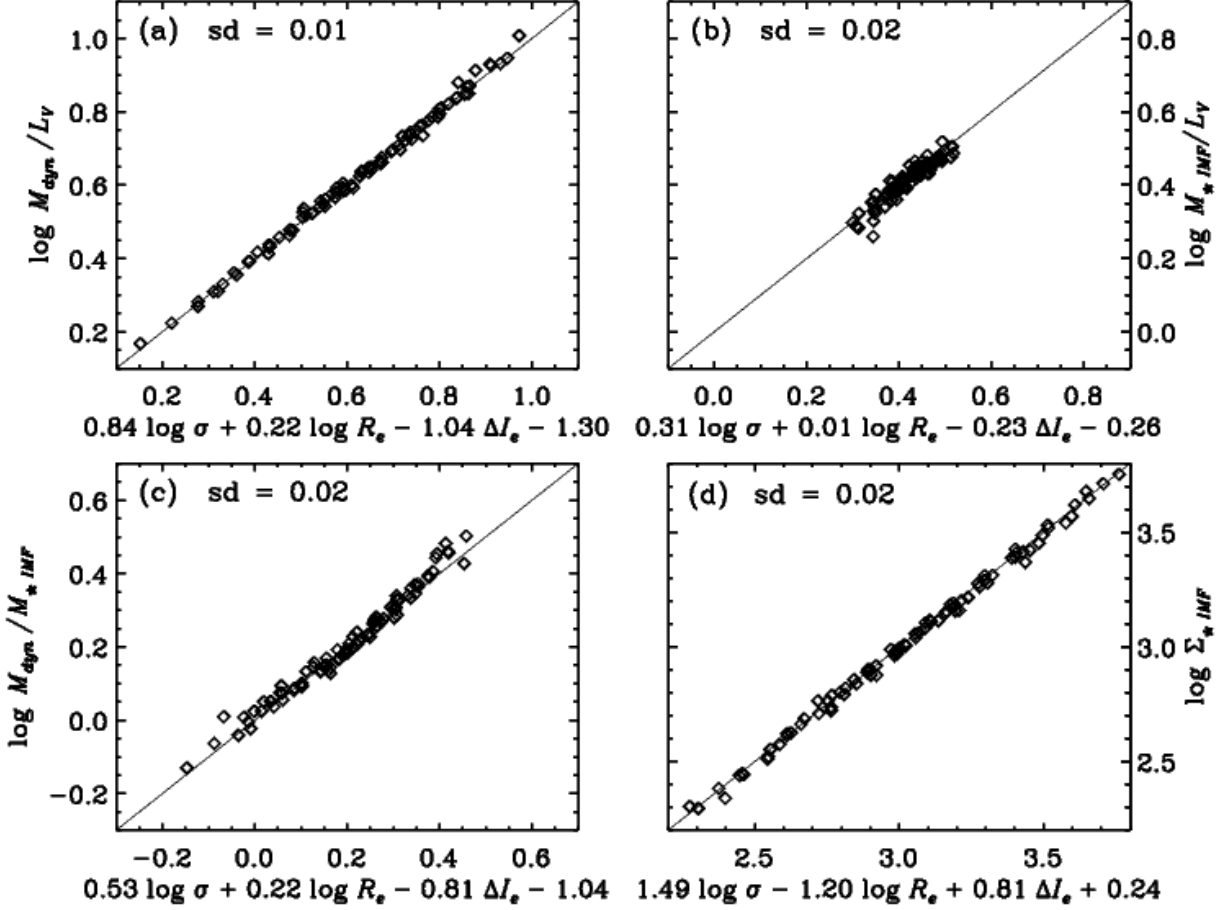


Figure 12. The quality of fits to (a) M_{dyn}/L_V , (b) $M_{*,IMF}/L_V$, (c) $M_{dyn}/M_{*,IMF}$, and (d) $\Sigma_{*,IMF}$ as functions of σ , R_e , and ΔI_e . In each panel, the median observed value of the parameter in question is plotted against the predicted value from the fits given in Table 2. Solid lines show the one-to-one relation. The standard deviation about the one-to-one relation is indicated in each panel and is ≤ 0.02 dex (i.e., $\leq 5\%$) for all four relations. The fits given in Table 2 are therefore excellent approximations to the measured values of all four mass parameters. These fits use the Gallazzi et al. (2005) values for $M_{*,IMF}/L$.

Table 3
Trend Directions for Stellar Population and Structural Properties

	Age (Gyr)	[Fe/H] (dex)	[Mg/H] (dex)	[Mg/Fe] (dex)	$\Sigma_{*,IMF}$ ($M_\odot \text{ pc}^{-2}$)	$M_{dyn}/M_{*,IMF}$ (M_\odot/M_\odot)	$M_{*,IMF}/L$ (M_\odot/L_\odot)	Δt_f (Gyr)
σ^*	+	+	+	+	+	+	+	-
R_e^\dagger	null	null	null	null	-	+	null	null
ΔI_e^\ddagger	-	+	+	-	+	-	-	+

Note. —

*Variations with σ along the FP, at fixed R_e .

†Variations with R_e along the FP, at fixed σ .

‡Variations with ΔI_e through the thickness of the FP, at fixed σ and fixed R_e .

the table indicates whether that property correlates (+) or anti-correlates (-) with σ (along the FP midplane at fixed R_e), with R_e (along the FP midplane at fixed σ), and with ΔI_e (through the thickness of the FP). The table also summarizes the results of this work by indicating how $\Sigma_{*,IMF}$, $M_{dyn}/M_{*,IMF}$, and $M_{*,IMF}/L$ vary with σ , R_e and ΔI_e . Lastly, the table includes an estimated trend in the duration of star formation (Δt_{SF}), based on the assumption that star formation timescale is inversely correlated with [Mg/Fe] (e.g., Tinsley 1979;

Greggio & Renzini 1983; Worthey et al. 1992; Matteucci 1994; Trager et al. 2000a; Thomas et al. 2005).

The following sections consider three families of mechanisms for producing $M_{dyn}/M_{*,IMF}$ variations, focusing on variations *through the thickness of the FP*. For each of these, we examine the implications for the stellar population properties and star formation histories of the galaxies, and compare these to the observations. We find that the full set of observations is best explained by a model that postulates the *premature truncation* of star forma-

Table 4
The Effects of Variable IMFs

	$M_*/M_{*,IMF}$ (M_\odot/M_\odot)	$\Delta \log I_e$ ($L_\odot \text{ pc}^{-2}$)	[Mg/Fe] (dex)	[Fe/H] (dex)	[Mg/H] (dex)
Observed*	+	−	+	−	−
More very high-mass stars	+	−	+	+	+
More very low-mass stars	+	−	none	−	−

Note. —

Assuming all variation is due to IMF differences, i.e., $M_{dyn}/M_ = const.$

tion in galaxies with high $M_{dyn}/M_{*,IMF}$ (and low I_e)—those that lie below the FP.

6.1. Variations in the IMF

The low- σ galaxies with high ΔI_e (upper left corner in Figure 10b) have $\log(M_{dyn}/M_{*,IMF}) \approx 0$, as can be read from the color-bar in that figure. This means that the stellar mass inferred using a Chabrier IMF can account for all of the mass detected dynamically. However, the rest of the galaxy bins have $\log(M_{dyn}/M_{*,IMF}) > 0$. If the entire discrepancy between M_{dyn} and $M_{*,IMF}$ through the thickness of the FP is due to IMF variations, then *all but the highest- ΔI_e galaxies must have formed with IMFs that produce less light for a given mass of stars formed than does the Chabrier IMF.*

There are two ways this could happen: through an excess of very low-mass stars that contribute substantially to M_* but produce very little light, or through an excess of massive stars at early times that create numerous compact remnants at late times, again contributing substantial mass but little light.

Variations in the IMF will also change the chemical enrichment history of a galaxy and predictions for this can be compared to the observed abundances. Table 4 summarizes the predictions for several different models and compares them to the observations. The SDSS galaxies show stellar population variations through the thickness of the FP such that galaxies with lower ΔI_e have higher [Mg/Fe], lower [Mg/H], and lower [Fe/H] than galaxies at the same σ and R_e with higher ΔI_e (Paper II). These trends are shown in the first row of Table 4.

An IMF which produces more massive stars ($> 8M_\odot$) at early times (and therefore more compact remnants at late times), in addition to having higher $M_*/M_{*,IMF}$ will produce a larger number of SNe II relative to SNe Ia. These galaxies should then have higher values of [Mg/Fe]. The large number of massive stars will also result in higher overall effective yields of both Mg and Fe, leading to higher values of [Mg/H] and [Fe/H], as summarized in the second row of Table 4. This combination of high [Mg/Fe] and higher effective yields does not match the observed stellar population variations through the thickness of the FP.

An IMF with an excess of low-mass stars could also produce high values of $M_*/M_{*,IMF}$, such as an IMF with Salpeter slope continuing down to low masses rather than turning over near $1M_\odot$, as in the Kroupa and Chabrier IMFs. Changing the fraction of stars below $\sim 1M_\odot$ would not affect the relative contributions of SNe II and SNe Ia but it would result in fewer SNe overall, thus significantly reducing the effective yields from both types of SNe. These lower yields are consistent with the lower

values of [Fe/H] and [Mg/H] observed in galaxies with high $M_{dyn}/M_{*,IMF}$, but this model does not reproduce the increase in [Mg/Fe] seen in such galaxies (see Table 4).

In general, it is difficult to simultaneously produce higher values of [Mg/Fe] and lower yields in both [Mg/H] and [Fe/H] by adjusting the IMF. This is because IMF modifications that produce a larger number of massive stars will tend to increase *both* [Mg/Fe] and the effective yield. This is not a problem when studying abundance trends along the FP, where [Mg/Fe], [Fe/H], and [Mg/H] all increase together with increasing σ (e.g., Table 3), but it presents a challenge when interpreting the trends through the thickness of the FP.

A possible way to save the IMF model is to assume that a larger proportion of massive stars will result in increased levels of SN feedback. Thus, although the raw yields will be higher in galaxies with more massive stars, a larger fraction of metal-enriched material may be removed through intense SN feedback. However, this involves an additional assumption about differences in feedback between galaxies. In what follows, we assume that the observed $M_{dyn}/M_{*,IMF}$ variations are dominated by real differences in dark matter fraction within R_e .

6.2. Variations in Inner Dark Matter Fraction: Redistributing Stars and Dark Matter through Merging

If dark-to-stellar mass ratio is really varying through the thickness of the FP, one of two statements must be true. Either galaxies with higher M_{dyn}/M_* are genuinely deficient in stellar mass for their halo size, or the overall stellar mass fractions are the same but stars are distributed differently such that the dark matter fraction *within* R_e is larger.¹⁸ We discuss the latter effect in this section; the former will be discussed in the next section.

Substantial dissipation during the galaxy formation process will lead to galaxies with centrally concentrated baryons, while less dissipation during formation will produce more extended stellar distributions. Such a process has been proposed by several authors as an explanation for the *tilt* of the FP. Here, we consider whether it might also contribute to the *thickness* of the FP.

The differential dissipation scenario was proposed more than a decade ago to explain differences in the kinematic structures of galaxies (Bender et al. 1992; Guzman et al. 1993; Ciotti et al. 1996; Faber et al. 1997). More recently, it has been modeled in the numerical simulations

¹⁸ The dynamical mass estimator M_{dyn} is predominantly sensitive to the mass inside R_e only.

of several groups (Oñorbe et al. 2005; Kobayashi 2005; Dekel & Cox 2006; Robertson et al. 2006) and invoked as an explanation for the tilt of the FP. The amount of dissipation during galaxy mergers is expected to be largest for low-mass galaxies, due to their higher gas fractions (e.g., Kannappan 2004), lower surface densities, and relatively long timescales for star formation (e.g., Noeske et al. 2007). With reasonable assumptions for the dependence of dissipation on galaxy mass, Robertson et al. (2006) and Dekel & Cox (2006) are able to reproduce the tilt of the FP as a function of M_* through variation in M_{dyn}/M_* . Recently, Covington (2008) has verified these results in a more realistic cosmological context by tracing galaxy properties through semi-analytic models of galaxy evolution, while Hopkins et al. (2008a) have found supporting observational evidence in the light profiles of nearby ellipticals. Once the FP has been established, further dissipationless merging will maintain the FP slope in isolated elliptical galaxies (Capelato et al. 1995; Dantas et al. 2003; Nipoti et al. 2003; Boylan-Kolchin et al. 2005; Robertson et al. 2006), although this is likely not true for brightest cluster galaxies (BCGs, e.g., Lauer et al. 2007).

We have argued above that variations in M_{dyn}/M_* are needed not only to reproduce the tilt of the FP, but its thickness as well. Suppose that these variations arise from different amounts of dissipation in the mergers that create different early type galaxies at fixed σ and R_e . As shown in Table 3, the galaxies with lower $M_{dyn}/M_{*,IMF}$ at fixed (σ, R_e) are the galaxies with younger mean ages and lower [Mg/Fe], consistent with their having more extended star formation histories. In this scenario, dissipational mergers with their accompanying bursts of star formation would have to occur preferentially in galaxies at later times, while early type galaxies that had star formation truncated early would have to have experienced a dissipationless merger.

However, this seems backwards to expectations, as galaxies at early times were in general more gas rich. Thus earlier mergers might be expected to be more dissipative, not less. In addition, the trends in $M_{dyn}/M_{*,IMF}$ and in stellar population properties continue unchanged down to small galaxies with $\sigma \approx 100 \text{ km s}^{-1}$ (see Figures 7–10 and Figures 7–10 of Paper II), where S0 galaxies are prevalent. Their low values of $M_{dyn}/M_{*,IMF}$ require them to have experienced a substantially dissipational merger under this scenario, after which they would have to regrow a disk and further quench star formation in the residual disk. It is not clear that this merger-driven mechanism can produce these smooth trends down to the modest galaxy masses included in this sample.

6.3. Variations in Inner Dark Matter Fraction: Low Efficiency Star Formation

The second scenario for variations in dark matter fraction consists of global differences in the stellar and dark matter mass fractions within a halo. In this scenario, a significant fraction of the baryonic material in some haloes does not get converted into stars. We will refer to this as a low “conversion efficiency” for the baryons. This conversion efficiency is known to vary with mass, such that M_*/M_{halo} has a maximum around the characteristic galaxy luminosity (L^* , Benson et al. 2000; Marinoni & Hudson 2002;

van den Bosch et al. 2003; Zaritsky et al. 2006) and from there decreases toward lower masses (e.g., dwarf galaxies) and toward higher masses (e.g., BCGs and galaxy clusters).

The galaxies in our sample are on the higher-mass side of this curve and should therefore have M_{halo}/M_* increasing with mass, i.e., their conversion efficiency of baryons into stars should *decrease* with increasing mass. The physical mechanism driving this change is thought to involve the truncation of star formation at some point in the evolution of the central galaxy, such that the galaxy halo continues to accrete mass but the incoming baryons are prevented from forming stars. It is very interesting that $M_{dyn}/M_{*,IMF}$ is observed to increase with M_{dyn} along the FP (e.g., Table 3). This increase in $M_{dyn}/M_{*,IMF}$ could well be the same phenomenon as the overall increase in M_{halo}/M_* , both of which appear to scale directly with mass. This suggests that the conversion efficiency within R_e may mimic the conversion efficiency of the parent halo as a whole.

As we did in the previous section with dissipational merging, we can invoke a process thought to cause $M_{dyn}/M_{*,IMF}$ variation along the FP to try to explain the variations through the thickness of the FP as well. The time at which star formation is truncated may vary among galaxies at the same σ and R_e , such that some galaxies have their star formation shut down prematurely, while other galaxies continue forming stars, accumulating more stellar mass, and further enriching their ISMs for extended periods of time.

This scenario of variable truncation times finally produces the consistent picture we have been looking for to explain all the trends observed through the thickness of the FP. Galaxies at fixed σ and R_e (i.e., fixed M_{dyn}) which are prematurely truncated wind up with shorter timescales for star formation (i.e., higher [Mg/Fe]), older mean ages, lower total stars formed (lower M_* and lower $\Sigma_{*,IMF}$), and incomplete processing of metals (lower [Fe/H] and lower [Mg/H]). In contrast, galaxies that are not truncated continue forming stars longer, resulting in longer star formation timescales (lower [Mg/Fe]), younger mean ages, more total stars (higher M_* and higher $\Sigma_{*,IMF}$), and more complete metal enrichment (higher [Fe/H] and [Mg/H]).

One possible truncation mechanism for satellites is the rapid quenching of star formation when a satellite falls into a massive halo and is stripped of gas (e.g., Gunn & Gott 1972; Lea & De Young 1976; Gislis 1976). This explanation predicts that galaxies with high $M_{dyn}/M_{*,IMF}$ (and therefore high [Mg/Fe]) at a given σ would tend to be satellites in more massive haloes today. However, there is some evidence that this type of quenching proceeds slowly in massive galaxies (e.g., Wolf et al. 2009) and may not be adequately abrupt to produce the high [Mg/Fe] seen in massive galaxies with high $M_{dyn}/M_{*,IMF}$. Moreover, many of our sample galaxies are central to their haloes—90.1% of our sample galaxies are identified as the most massive galaxies in their haloes in the Yang et al. (2007) group catalogs—and thus satellite quenching processes are not relevant for them.

Another possible truncation mechanism is very powerful feedback, in which a substantial quantity of the interstellar medium (ISM) is heated and removed from the galaxy potential well before it can form

stars. Both starburst-driven outflows (with velocities up to $\sim 600 \text{ km s}^{-1}$ Heckman et al. 2000) and AGN-driven outflows (which can reach velocities in excess of $\sim 1000 \text{ km s}^{-1}$ Trump et al. 2006) may be able to unbind gas from galaxies. Theoretical frameworks for AGN feedback in particular have been provided by many authors (e.g., Granato et al. 2004; Scannapieco & Oh 2004; Di Matteo et al. 2005; Springel et al. 2005; Hopkins et al. 2008b). Real life examples of AGN feedback could include the two massive $z \approx 3.5$ galaxies discussed in Nesvadba et al. (2007). They present optical and radio observations the strong radio jets observed in these systems and calculate that the mass-loading of the jet material may represent several times $10^{10} M_{\odot}$ of ISM. Such objects may be evidence of powerful AGN feedback in action. SN-driven outflows may also be able to quench star formation in early type galaxies (e.g., Pipino et al. 2008), although there is some evidence that the outflow velocities in identifiable post-starburst galaxies require the presence of an AGN (Tremonti et al. 2007).

A variation on feedback-induced truncation could be supernova feedback in smaller galaxies that then assemble into larger galaxies. Galaxies with high $M_{dyn}/M_{*,IMF}$ could be galaxies that did not form the majority of their stars *in situ*, but instead assembled hierarchically at early times from many smaller galaxies. These small galaxies might have shallow enough potential wells that supernova feedback can play an important role in removing baryons (White & Rees 1978; Dekel & Silk 1986; White & Frenk 1991; Benson et al. 2003). This process could shut down star formation at earlier times and lead to the observed older ages and higher [Mg/Fe] of their massive descendants, as compared to galaxies at the same σ with lower $M_{dyn}/M_{*,IMF}$, which may have formed more of their stars *in situ* in massive haloes. A galaxy which formed in many smaller pieces would also have lower metallicity, both because its ISM experienced fewer generations of stellar processing resulting in a lower effective yield, and because SN feedback would be more effective at removing metal-enriched gas from the galaxy. In this scenario, the galaxies that form in smaller pieces would also have to form at earlier times (to match the observed age trends).

Yet another mechanism is quenching by massive haloes (e.g., Birnboim & Dekel 2003; Cattaneo et al. 2008), when halos pass over a critical mass threshold (M_{crit}) and shock-heated gas accreting onto them can no longer cool efficiently. Variations through the FP could be due to stochastic variations in the halo mass assembly history, if galaxies with the same σ and R_e today exist in halos that passed over M_{crit} at different times, or if mass was accreted differently onto these halos, affecting the cooling rate. This would mean that halo mass is not perfectly coupled to the structure of the visible galaxy. Also, halo-quenching scenarios need to be coupled with some kind of maintenance mode to suppress star formation, such as “radio-mode” AGN activity (e.g., Croton et al. 2006).

All of these scenarios of truncated star formation are qualitatively consistent with the higher values of [Mg/Fe], lower effective yields, and hypothesized shorter-duration star formation histories of high $M_{dyn}/M_{*,IMF}$ galaxies. Indeed, low-efficiency star formation due to

truncation is an attractive solution to simultaneously achieving high [Mg/Fe], low effective yields, and lower total production of stars. Semi-analytic models of galaxy formation may provide clues as to which, if any, of these mechanisms can produce quantitative agreement with the observed galaxy properties.

7. CONCLUSIONS

In Paper II, we demonstrated that the stellar population properties, and therefore the star formation histories, of quiescent early type galaxies form a two-parameter family. These map onto a cross-section through the Fundamental Plane. In this paper, we have explored the associated mass-to-light variations in 3D FP space. This has allowed us to map out the various components of mass-to-light variation both along the FP and through its thickness, with the following results:

1. We map M_{dyn}/L , $M_{dyn}/M_{*,IMF}$, and $M_{*,IMF}/L$ throughout 3D Fundamental Plane space. These quantities can be well-approximated by first-order functions (i.e., hyperplane fits) of $\log \sigma$, $\log R_e$, and $\Delta \log I_e$. These fits are provided in Table 2.
2. We confirm that the variation in $M_{*,IMF}/L$ due to stellar population variations cannot account for the tilt of the FP, as demonstrated by many previous authors. Variations in the dark matter fraction within R_e (i.e., M_{dyn}/M_{*}) or in the IMF (i.e., $M_{*}/M_{*,IMF}$) are required to explain the tilt of the FP. Using the $M_{*,IMF}$ estimates of Gallazzi et al. (2005), stellar population effects contribute only 1/3 of the tilt of the FP, while dark matter/IMF effects contribute the remaining 2/3.
3. The stellar population and the dark matter/IMF contributions to the FP tilt rotate the plane around different axes in the 3D space, with $M_{*,IMF}/L \propto f(\sigma)$, while $M_{dyn}/M_{*,IMF} \propto g(M_{dyn})$.
4. Although Paper II showed that stellar populations vary through the thickness of the FP (in agreement with Forbes et al. 1998, Wuyts et al. 2004, and Gargiulo et al. 2009), the associated variations in $M_{*,IMF}/L$ alone *cannot account for the thickness of the FP*. Variations in the dark matter contribution within R_e (i.e., M_{dyn}/M_{*}) or in the IMF (i.e., $M_{*}/M_{*,IMF}$) are required to explain the thickness of the FP (as well as the tilt). Using the $M_{*,IMF}$ estimates of Gallazzi et al. (2005), stellar population effects contribute only 22% of the thickness of the FP, while dark matter/IMF effects contribute the remaining 78%.
5. Because stellar population effects contribute only $\sim 22\%$ of the thickness of the FP, the observed M_{dyn}/L variations through the plane are dominated by variations in $\Sigma_{*,IMF}$. This means that galaxies do not move below the plane by fading; they either form initially with lower $\Sigma_{*,IMF}$ or move there due to *structural* changes in the stellar mass distribution.
6. Combining the results of this work with the results of Paper II, we find that variations in the

dark matter/IMF contribution through the thickness of the FP are associated with differences in galaxy star formation histories. The correlation is such that galaxies with higher $M_{dyn}/M_{*,IMF}$ also have higher [Mg/Fe], older ages, and lower metallicities than their lower- $M_{dyn}/M_{*,IMF}$ counterparts at the same σ , which may indicate that the higher- $M_{dyn}/M_{*,IMF}$ galaxies have experienced shorter duration star formation. Possible physical mechanisms for producing high- $M_{dyn}/M_{*,IMF}$ and the associated stellar population variations include:

- a) A top-heavy IMF in some galaxies, which produces more SNe II relative to SNe Ia and therefore higher [Mg/Fe]. However, this scenario does not simultaneously produce the observed lower [Fe/H] and [Mg/H] in these galaxies. Invoking IMF variations to explain the observed $M_{dyn}/M_{*,IMF}$ variations would require an additional physical mechanism, such as enhanced SN feedback that removes a substantial fraction of the metal-enriched material.
 - b) Higher dark matter fraction within R_e due to low-dissipation merging in galaxies that have already quenched their star formation. This scenario is plausible, but the predicted trend with stellar population age seems backwards to expectations since early-forming galaxies are naturally more gas-rich, not less.
 - c) Low conversion efficiency of baryons into stars through the premature truncation of star formation. There are various possible mechanisms for this truncation, including ram-pressure stripping in satellite galaxies, powerful AGN feedback, massive halo quenching, or low-mass progenitor galaxies that are strongly affected by supernova feedback (as compared to galaxies that form most of their stars *in situ* in deep potential wells). This truncation scenario is appealing because it simultaneously matches the lower stellar masses, older ages, higher [Mg/Fe], lower [Fe/H], and lower [Mg/H] observed in the high- $M_{dyn}/M_{*,IMF}$ galaxies at fixed σ .
7. There is an intriguing parallel between the known increase of M_{halo}/M_* in large haloes and the increase in $M_{dyn}/M_{*,IMF}$ along the FP observed in this galaxy sample. This suggests that the conversion efficiency of baryons into stars inside R_e mimics the overall conversion efficiency for the parent halo. The truncation of star formation in massive galaxies is widely accepted as the explanation for the increase in M_{halo}/M_* with galaxy mass, although the truncation *mechanism* is debated. It may be that this same truncation mechanism also produces differences in conversion efficiency *inside* R_e , and that this effect drives the observed variation in $M_{dyn}/M_{*,IMF}$ through the thickness of the FP as well.

These results have focused on quiescent galaxies only, excluding early type galaxies with ongoing star formation, Seyfert, or LINER activity. Seyfert and

LINER hosts are known to have systematically younger stellar population ages than their quiescent counterparts (Kauffmann et al. 2003a; Graves et al. 2007; Schawinski et al. 2007), but further analysis is required to determine whether they follow the other stellar population and M/L trends explored here for quiescent galaxies.

Taken as an ensemble, the results presented in this series of papers illustrate a connection between the star formation histories and the present-day mass structures of early type galaxies. As such, they represent a stringent test for models of galaxy formation and a challenge for the next generation of semi-analytic models. They also highlight the emerging importance of abundances in testing model star formation histories. Paper IV makes extensive use of this abundance information to expand on and quantify the premature truncation model proposed here.

The authors would like to thank Renbin Yan for providing the emission line measurements used to identify the sample of early-type galaxies used here. This work was supported by National Science Foundation grant AST 05-07483. G. G. is supported by a fellowship from the Miller Institute for Basic Research in Science. G. G. also acknowledges support from the ARCS Foundation and from a UCSC Dissertation Year Fellowship

Funding for the creation and distribution of the SDSS Archive has been provided by the Alred P. Sloan Foundation, the Participating Institutions, the National Aeronautics and Space Administration, the National Science Foundation, the US Department of Energy, the Japanese Monbukagakusho, and the Max-Planck Society. The SDSS Web site is <http://www.sdss.org/>.

The SDSS is managed by the Astrophysical Research Consortium (ARC) for the Participating Institutions. The Participating Institutions are the University of Chicago, Fermilab, the Institute for Advanced Study, the Japan Participation Group, the Johns Hopkins University, the Korean Scientist Group, Los Alamos National Laboratory, the Max-Planck-Institute for Astronomy (MPIA), the Max-Planck-Institute for Astrophysics (MPA), New Mexico State University, University of Pittsburgh, University of Portsmouth, Princeton University, the United States Naval Observatory, and the University of Washington.

REFERENCES

- Adelman-McCarthy, J. K., et al. 2006, ApJS, 162, 38
Allanson, S. P., Hudson, M. J., Smith, R. J., & Lucey, J. R. 2009, ApJ, 702, 1275
Balogh, M. L., Morris, S. L., Yee, H. K. C., Carlberg, R. G., & Ellingson, E. 1999, ApJ, 527, 54
Bell, E. F., McIntosh, D. H., Katz, N., & Weinberg, M. D. 2003, ApJS, 149, 289
Bender, R., Burstein, D., & Faber, S. M. 1992, ApJ, 399, 462
Benson, A. J., Bower, R. G., Frenk, C. S., Lacey, C. G., Baugh, C. M., & Cole, S. 2003, ApJ, 599, 38
Benson, A. J., Cole, S., Frenk, C. S., Baugh, C. M., & Lacey, C. G. 2000, MNRAS, 311, 793
Bernardi, M., et al. 2003a, AJ, 125, 1817
—, 2003b, AJ, 125, 1866
Birnboim, Y., & Dekel, A. 2003, MNRAS, 345, 349
Blanton, M. R., & Roweis, S. 2007, AJ, 133, 734
Blanton, M. R., et al. 2005, AJ, 129, 2562

- Bolton, A. S., Burles, S., Treu, T., Koopmans, L. V. E., & Moustakas, L. A. 2007, *ApJ*, 665, L105
- Bolton, A. S., Treu, T., Koopmans, L. V. E., Gavazzi, R., Moustakas, L. A., Burles, S., Schlegel, D. J., & Wayth, R. 2008, *ApJ*, 684, 248
- Boylan-Kolchin, M., Ma, C.-P., & Quataert, E. 2005, *MNRAS*, 362, 184
- Bruzual, G., & Charlot, S. 2003, *MNRAS*, 344, 1000
- Capelato, H. V., de Carvalho, R. R., & Carlberg, R. G. 1995, *ApJ*, 451, 525
- Cappellari, M., et al. 2006, *MNRAS*, 366, 1126
- Cardiel, N., Gorgas, J., Cenarro, J., & Gonzalez, J. J. 1998, *A&AS*, 127, 597
- Cattaneo, A., Dekel, A., Faber, S. M., & Guiderdoni, B. 2008, *MNRAS*, 389, 567
- Chabrier, G. 2003, *PASP*, 115, 763
- Chiosi, C., Bressan, A., Portinari, L., & Tantalo, R. 1998, *A&A*, 339, 355
- Ciotti, L., & Lanzoni, B. 1997, *A&A*, 321, 724
- Ciotti, L., Lanzoni, B., & Renzini, A. 1996, *MNRAS*, 282, 1
- Covington, M. D. 2008, PhD thesis, University of California, Santa Cruz
- Croton, D. J., et al. 2006, *MNRAS*, 365, 11
- Dantas, C. C., Capelato, H. V., Ribeiro, A. L. B., & de Carvalho, R. R. 2003, *MNRAS*, 340, 398
- de Carvalho, R., de La Rosa, I., & Zepf, S. 2003, *Ap&SS*, 285, 79
- de la Rosa, I. G., de Carvalho, R. R., & Zepf, S. E. 2001, *AJ*, 122, 93
- Dekel, A., & Cox, T. J. 2006, *MNRAS*, 370, 1445
- Dekel, A., & Silk, J. 1986, *ApJ*, 303, 39
- Di Matteo, T., Springel, V., & Hernquist, L. 2005, *Nature*, 433, 604
- Djorgovski, S., & Davis, M. 1987, *ApJ*, 313, 59
- Dotter, A., Chaboyer, B., Ferguson, J. W., Lee, H.-c., Worthey, G., Jevremović, D., & Baron, E. 2007, *ApJ*, 666, 403
- Dressler, A., Lynden-Bell, D., Burstein, D., Davies, R. L., Faber, S. M., Terlevich, R., & Wegner, G. 1987, *ApJ*, 313, 42
- Faber, S. M., Dressler, A., Davies, R. L., Burstein, D., & Lynden-Bell, D. 1987, in *Nearly Normal Galaxies. From the Planck Time to the Present*, ed. S. M. Faber, 175–183
- Faber, S. M., & Jackson, R. E. 1976, *ApJ*, 204, 668
- Faber, S. M., et al. 1997, *AJ*, 114, 1771
- Fioc, M., & Rocca-Volmerange, B. 1997, *A&A*, 326, 950
- Forbes, D. A., Ponman, T. J., & Brown, R. J. N. 1998, *ApJ*, 508, L43
- Fritz, A., Ziegler, B. L., Bower, R. G., Smail, I., & Davies, R. L. 2005, *MNRAS*, 358, 233
- Gallazzi, A., Charlot, S., Brinchmann, J., White, S. D. M., & Tremonti, C. A. 2005, *MNRAS*, 362, 41
- Gargiulo, A., et al. 2009, *MNRAS*, 397, 75
- Gebhardt, K., et al. 2003, *ApJ*, 597, 239
- Gisler, G. R. 1976, *A&A*, 51, 137
- Granato, G. L., De Zotti, G., Silva, L., Bressan, A., & Danese, L. 2004, *ApJ*, 600, 580
- Graves, G. J., Faber, S. M., & Schiavon, R. P. 2009a, *ApJ*, 693, 486
- . 2009b, *ApJ*, 698, 1590
- Graves, G. J., Faber, S. M., Schiavon, R. P., & Yan, R. 2007, *ApJ*, 671, 243
- Graves, G. J., & Schiavon, R. P. 2008, *ApJS*, 177, 446
- Greggio, L., & Renzini, A. 1983, *Memorie della Societa Astronomica Italiana*, 54, 311
- Gunn, J. E., & Gott, J. R. I. 1972, *ApJ*, 176, 1
- Guzman, R., Lucey, J. R., & Bower, R. G. 1993, *MNRAS*, 265, 731
- Heckman, T. M., Lehnert, M. D., Strickland, D. K., & Armus, L. 2000, *ApJS*, 129, 493
- Holden, B. P., et al. 2005, *ApJ*, 620, L83
- Hopkins, P. F., Cox, T. J., & Hernquist, L. 2008a, *ApJ*, 689, 17
- Hopkins, P. F., Cox, T. J., Kereš, D., & Hernquist, L. 2008b, *ApJS*, 175, 390
- Hyde, J. B., & Bernardi, M. 2009, *MNRAS*, 396, 1171
- Jørgensen, I., Chiboucas, K., Flint, K., Bergmann, M., Barr, J., & Davies, R. 2006, *ApJ*, 639, L9
- Jørgensen, I., Franx, M., Hjorth, J., & van Dokkum, P. G. 1999, *MNRAS*, 308, 833
- Jørgensen, I., Franx, M., & Kjaergaard, P. 1995, *MNRAS*, 276, 1341
- . 1996, *MNRAS*, 280, 167
- Jun, H. D., & Im, M. 2008, *ApJ*, 678, L97
- Kannappan, S. J. 2004, *ApJ*, 611, L89
- Kauffmann, G., et al. 2003a, *MNRAS*, 346, 1055
- . 2003b, *MNRAS*, 341, 33
- Kelson, D. D., van Dokkum, P. G., Franx, M., Illingworth, G. D., & Fabricant, D. 1997, *ApJ*, 478, L13
- Kennicutt, Jr., R. C. 1998, *ARA&A*, 36, 189
- Kobayashi, C. 2005, *MNRAS*, 361, 1216
- Kochanek, C. S., et al. 2000, *ApJ*, 543, 131
- Koopmans, L. V. E., et al. 2009, *ApJ*, 703, L51
- Kormendy, J. 1985, *ApJ*, 295, 73
- Kroupa, P. 2001, *MNRAS*, 322, 231
- La Barbera, F., Busarello, G., Merluzzi, P., de la Rosa, I. G., Coppola, G., & Haines, C. P. 2008, *ApJ*, 689, 913
- Lauer, T. R. 1985, *ApJ*, 292, 104
- Lauer, T. R., et al. 2007, *ApJ*, 662, 808
- Lea, S. M., & De Young, D. S. 1976, *ApJ*, 210, 647
- Lee, H., Worthey, G., & Blakeslee, J. P. 2010, *ApJ*, 710, 421
- Longhetti, M., & Saracco, P. 2009, *MNRAS*, 394, 774
- Maraston, C. 2005, *MNRAS*, 362, 799
- Maraston, C., Strömbäck, G., Thomas, D., Wake, D. A., & Nichol, R. C. 2009, *MNRAS*, 394, L107
- Marinoni, C., & Hudson, M. J. 2002, *ApJ*, 569, 101
- Markwardt, C. B. 2009, in *ASP Conf. Ser.*, Vol. 411, *ASP Conf. Ser.*, ed. D. A. Bohlender, D. Durand, & P. Dowler, 251
- Matteucci, F. 1994, *A&A*, 288, 57
- Mobasher, B., Guzman, R., Aragon-Salamanca, A., & Zepf, S. 1999, *MNRAS*, 304, 225
- Nesvadba, N. P. H., Lehnert, M. D., De Breuck, C., Gilbert, A., & van Breugel, W. 2007, *A&A*, 475, 145
- Nipoti, C., Londrillo, P., & Ciotti, L. 2002, *MNRAS*, 332, 901
- . 2003, *MNRAS*, 342, 501
- Noeske, K. G., et al. 2007, *ApJ*, 660, L47
- Oñorbe, J., Domínguez-Tenreiro, R., Sáiz, A., Serna, A., & Artal, H. 2005, *ApJ*, 632, L57
- Padmanabhan, N., et al. 2004, *New Astronomy*, 9, 329
- Pahre, M. A., Djorgovski, S. G., & de Carvalho, R. R. 1995, *ApJ*, 453, L17
- . 1998, *AJ*, 116, 1591
- Pahre, M. A., Djorgovski, S. G., & De Carvalho, R. R. 2001, *Ap&SS*, 276, 983
- Pipino, A., D’Ercole, A., & Matteucci, F. 2008, *A&A*, 484, 679
- Prugniel, P., & Simien, F. 1996, *A&A*, 309, 749
- . 1997, *A&A*, 321, 111
- Reda, F. M., Forbes, D. A., & Hau, G. K. T. 2005, *MNRAS*, 360, 693
- Renzini, A., & Ciotti, L. 1993, *ApJ*, 416, L49
- Robertson, B., Cox, T. J., Hernquist, L., Franx, M., Hopkins, P. F., Martini, P., & Springel, V. 2006, *ApJ*, 641, 21
- Salpeter, E. E. 1955, *ApJ*, 121, 161
- Scannapieco, E., & Oh, S. P. 2004, *ApJ*, 608, 62
- Schawinski, K., Thomas, D., Sarzi, M., Maraston, C., Kaviraj, S., Joo, S.-J., Yi, S. K., & Silk, J. 2007, *MNRAS*, 382, 1415
- Schiavon, R. P. 2007, *ApJS*, 171, 146
- Schlegel, D. J., Finkbeiner, D. P., & Davis, M. 1998, *ApJ*, 500, 525
- Scoddeggio, M., Gavazzi, G., Belsole, E., Pierini, D., & Boselli, A. 1998, *MNRAS*, 301, 1001
- Silva, L., Granato, G. L., Bressan, A., & Danese, L. 1998, *ApJ*, 509, 103
- Smith, R. J., Lucey, J. R., Hudson, M. J., & Bridges, T. J. 2009, *MNRAS*, 398, 119
- Springel, V., et al. 2005, *Nature*, 435, 629
- Stoughton, C., et al. 2002, in *SPIE*, Vol. 4836, *Survey and Other Telescope Technologies and Discoveries.*, ed. J. A. Tyson & S. Wolff, 339–349
- Strauss, M. A., et al. 2002, *AJ*, 124, 1810
- Thomas, D., Maraston, C., Bender, R., & Mendes de Oliveira, C. 2005, *ApJ*, 621, 673
- Tinsley, B. M. 1979, *ApJ*, 229, 1046
- . 1981, *MNRAS*, 194, 63
- Trager, S. C., Faber, S. M., Worthey, G., & González, J. J. 2000a, *AJ*, 120, 165
- . 2000b, *AJ*, 119, 1645

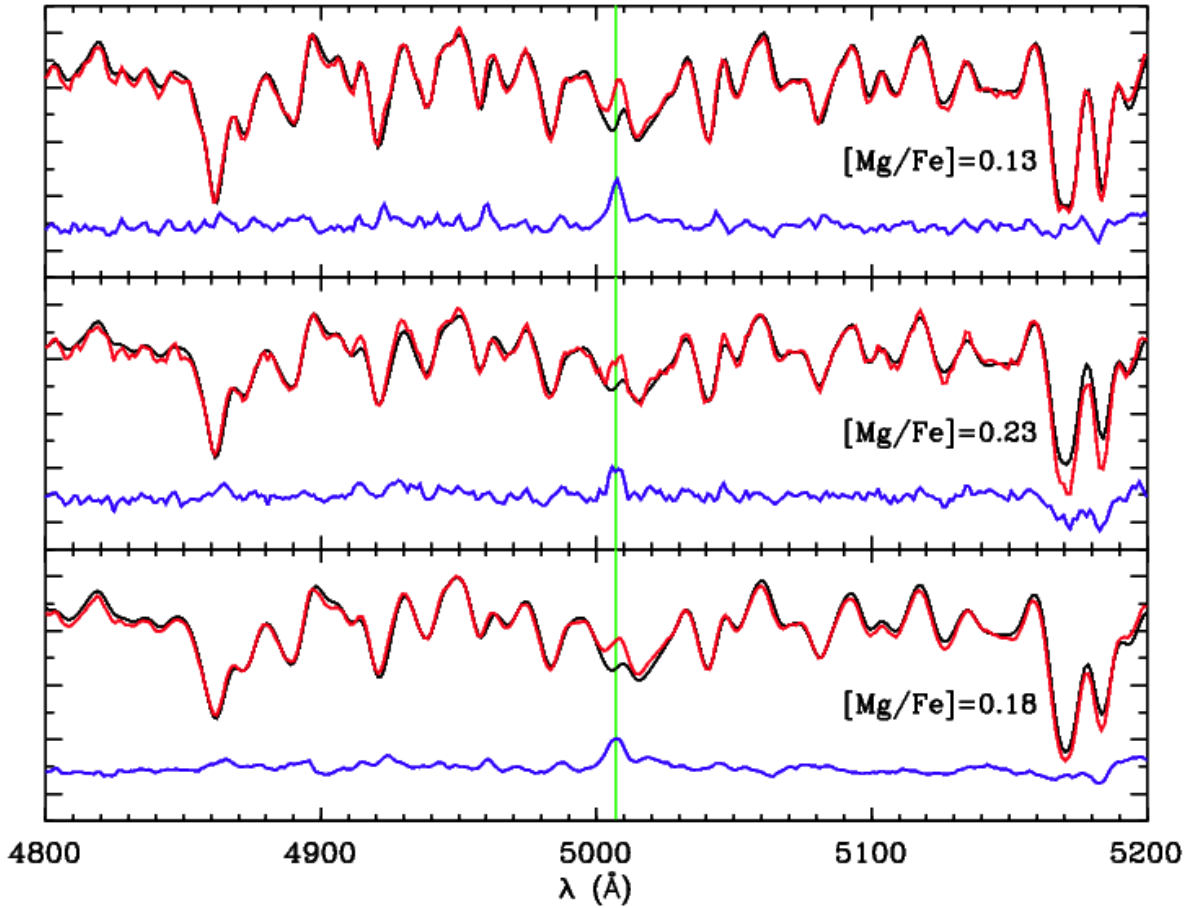


Figure 13. Three examples of weak $[\text{OIII}]\lambda 5007$ emission in the stacked spectra. In each panel, the thick black line shows the data, the thin gray line shows the BC03 model with the closest match in age and $[\text{Fe}/\text{H}]$, and the lower dark gray line shows the difference between the data and the model. The vertical line indicates the location of the $[\text{OIII}]\lambda 5007$ emission line, which is weak but clearly detected in all cases. The data have, from top to bottom, $\log \sigma = 2.06$, $\log \sigma = 2.14$, and $\log \sigma = 2.23$, with the models smoothed to match the combined SDSS spectral resolution and intrinsic velocity dispersion of the data. The BC03 models have a fixed abundance pattern, while many of the sample galaxies have substantially super-solar $[\text{Mg}/\text{Fe}]$ (as labelled). This causes a mismatch between the data and models around the 5190 Å Mg absorption feature but does not seriously bias the fit to most of the spectrum, which is dominated by Fe absorption features.

Tremonti, C. A., Moustakas, J., & Diamond-Stanic, A. M. 2007, *ApJ*, 663, L77
 Treu, T., Auger, M. W., Koopmans, L. V. E., Gavazzi, R., Marshall, P. J., & Bolton, A. S. 2010, *ApJ*, 709, 1195
 Treu, T., Stiavelli, M., Bertin, G., Casertano, S., & Møller, P. 2001, *MNRAS*, 326, 237
 Trujillo, I., Burkert, A., & Bell, E. F. 2004, *ApJ*, 600, L39
 Trump, J. R., et al. 2006, *ApJS*, 165, 1
 van de Ven, G., van Dokkum, P. G., & Franx, M. 2003, *MNRAS*, 344, 924
 van den Bosch, F. C., Yang, X., & Mo, H. J. 2003, *MNRAS*, 340, 771
 van der Marel, R. P., & van Dokkum, P. G. 2007, *ApJ*, 668, 756
 White, S. D. M., & Frenk, C. S. 1991, *ApJ*, 379, 52

White, S. D. M., & Rees, M. J. 1978, *MNRAS*, 183, 341
 Wolf, J., Martinez, G. D., Bullock, J. S., Kaplinghat, M., Geha, M., Munoz, R. R., Simon, J. D., & Avedo, F. F. 2009, ArXiv e-prints
 Worthey, G., Faber, S. M., & Gonzalez, J. J. 1992, *ApJ*, 398, 69
 Worthey, G., & Ottaviani, D. L. 1997, *ApJS*, 111, 377
 Wuyts, S., van Dokkum, P. G., Kelson, D. D., Franx, M., & Illingworth, G. D. 2004, *ApJ*, 605, 677
 Yan, R., Newman, J. A., Faber, S. M., Konidaris, N., Koo, D., & Davis, M. 2006, *ApJ*, 648, 281
 Yang, X., Mo, H. J., van den Bosch, F. C., Pasquali, A., Li, C., & Barden, M. 2007, *ApJ*, 671, 153
 Zaritsky, D., Gonzalez, A. H., & Zabludoff, A. I. 2006, *ApJ*, 638, 725

APPENDIX

CORRECTING FOR LOW-LEVEL $\text{H}\beta$ EMISSION INFILL

The galaxies presented here are selected to contain no ionized gas emission by requiring that the strong emission lines at $\text{H}\alpha$ and $[\text{OII}]\lambda 3727$ be undetected at the 2σ level. This results in a sample of quiescent galaxies that lack both significant ongoing star formation and AGN/LINER activity.

The individual SDSS spectra have relatively low S/N . Our sample therefore contains galaxies with weak emission below the detection threshold in individual galaxies. Weak $\text{H}\beta$ emission will partially fill in the $\text{H}\beta$ absorption feature used to determine galaxy ages, causing the stellar population modelling to return ages that are too old. Even small errors in $\text{H}\beta$ can result in significant overestimates of the galaxy ages; at 10 Gyr, 0.1 Å in $\text{H}\beta$ corresponds to an

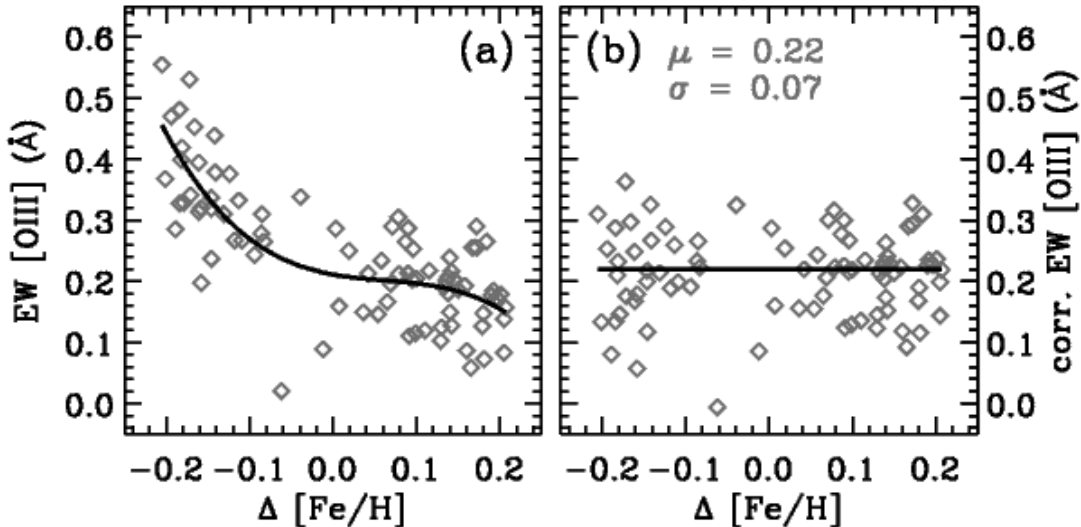


Figure 14. (a) The EW of [OIII] λ 5007 as a function of the offset in [Fe/H] between the measured [Fe/H] of the data and the closest-matching BC03 model. Mismatches in [Fe/H] between the data and the model cause biases in the estimates of [OIII]. We use a third-degree polynomial fit (solid line) to fit the trend in [OIII] with Δ [Fe/H] and correct the [OIII] measurements to the values that they would have if Δ [Fe/H]=0 for the entire sample (b). The mean and standard deviation of the corrected [OIII] EW measurements are given.

age difference of roughly 1 Gyr (Schiavon 2007). However, if weak emission can be detected in the high- S/N stacked spectra, a correction for this effect can be applied to the measured values of $H\beta$, resulting in more accurate age measurements.

We do this by measuring the equivalent width (EW) of emission in the [OIII] λ 5007 line and using the relation

$$\Delta H\beta = 0.7EW([\text{OIII}]\lambda 5007) \quad (\text{A1})$$

suggested by Trager et al. (2000b). Using the sample of Graves et al. (2007), we have confirmed that this relation is a good approximation for the line ratios of LINERs, which likely make up the majority of weak emission-line objects in our sample (Yan et al. 2006, see also Figure 7b of that work).

To measure $EW[\text{OIII}]$, we restack all of the composite spectra without smoothing the spectra to $\sigma = 300 \text{ km s}^{-1}$. A weak, narrow emission feature should be easier to detect if it is not smoothed up to the maximum velocity dispersion of the sample. In practice, the width of [OIII] appears to track the stellar σ closely, such that the emission in high- σ galaxies is substantially broader than the emission in low- σ galaxies, although the integrated EW is similar.

For each stacked spectrum, we identify the BC03 model with the closest match to the age and [Fe/H] values measured in our stellar population analysis. The BC03 models sample parameter space fairly densely in age, but only sparsely in [Fe/H], so that the age mismatch between data and model is less than 0.02 dex, while the mismatch in [Fe/H] can be as much as 0.2 dex. Three examples with different σ values are shown in Figure 13. We divide out the continua of the data and the model, smooth the model to match the combined SDSS resolution and intrinsic σ of the stacked spectrum, and compare the data (red line) and model (black line) in the 4800–5200 Å range.

The models are an excellent match to the data except in two locations: [OIII] emission, though weak, is clearly visible at 5007 Å in the data but is not included in the models, and the data show stronger absorption in the Mg feature at 5190 Å than is predicted in the models. The latter effect is due to the fact that the BC03 models have a fixed solar abundance pattern, while early type galaxies typically have super-solar [Mg/Fe]. The larger the measured value of [Mg/Fe], the bigger the mismatch between data and model at 5190 Å. The mismatch in the abundance pattern does not seriously bias the fit to the rest of the spectrum, which is dominated by Fe absorption features.

To measure [OIII], we compute the difference spectrum between the data and the model (blue line) and integrate the residual [OIII] flux, using the bandpass and continuum definitions of Yan et al. (2006). The detection of [OIII] emission implies that $H\beta$ emission is also present, filling in the stellar $H\beta$ absorption line. This $H\beta$ infill is not visible because the chosen BC03 model has been matched to the mean age of the *uncorrected* stacked spectrum.

As mentioned above, the BC03 models are only computed for a limited set of [Fe/H] values and are therefore not always well-matched to the data. Metallicity offsets between the data and the model can bias the measurement of $EW([\text{OIII}])$. Figure 14a shows the measured value of $EW([\text{OIII}])$ as a function of the offset between [Fe/H] as measured in the data and the closest-matched BC03 model. Compared to galaxies that are well-matched to the models (Δ [Fe/H] \approx 0), galaxies for which the best-fitting model is at higher metallicity (Δ [Fe/H] < 0) or lower metallicity (Δ [Fe/H] > 0) produce $EW([\text{OIII}])$ measurements that are significantly overestimated or underestimated, respectively.

To correct our $EW([\text{OIII}])$ measurements to the value they would have if a perfectly-matched model were available, we fit a third-degree polynomial to the data in Figure 14a and subtract out the trend with Δ [Fe/H] to produce corrected $EW([\text{OIII}])$ values (Figure 14b). The corrected $EW([\text{OIII}])$ measurements have a roughly Gaussian distribution with

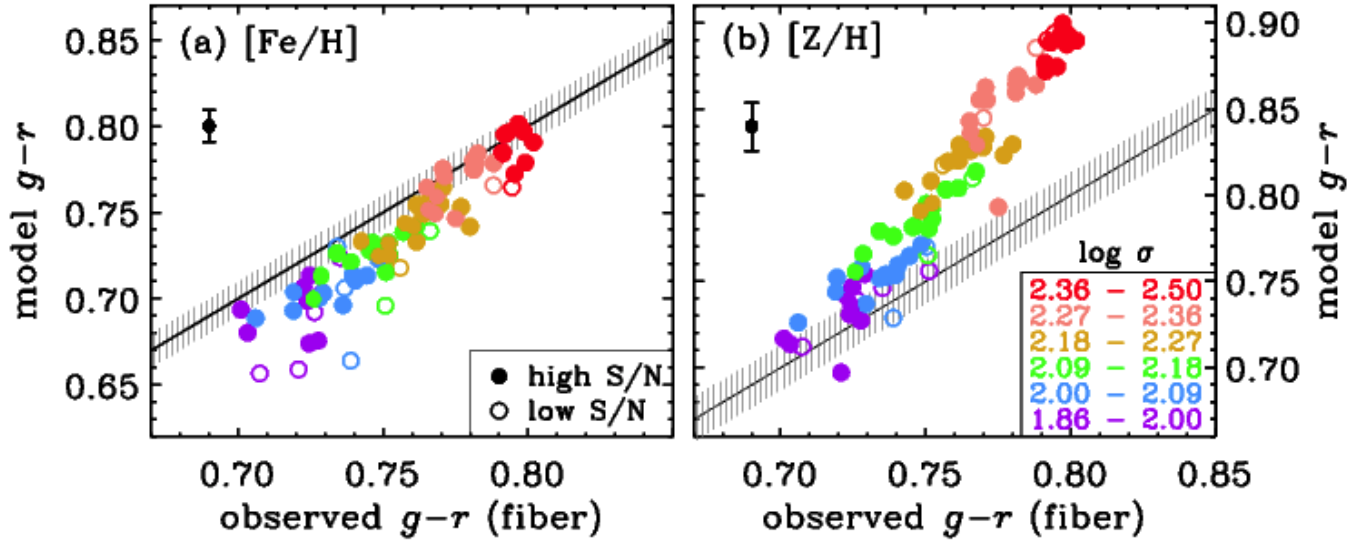


Figure 15. (a) A comparison of the $g-r$ colors derived from stellar population modelling with the observed $g-r$ colors as measured from photometry matched to the $3''$ SDSS spectral fiber aperture. Model $g-r$ colors are derived by matching the age and $[\text{Fe}/\text{H}]$ measured for the stacked galaxy spectra to BC03 models, as illustrated in Figure 4b. The line shows a one-to-one relation, with shading indicating the typical 1σ scatter expected due to absorption line measurement errors. Data with substantially larger errors are shown as open circles. For high- σ galaxies, the model colors are an excellent match to the observed colors, with observed colors showing ≤ 0.02 mag of internal reddening that is not included in the models. The discrepancy is larger for low- σ galaxies, suggesting that single burst models systematically underestimate the mean stellar population ages for younger galaxies (see text for details). (b) The same as (a), but with models derived by matching the age and $[\text{Z}/\text{H}]$ measured in the stacked spectra. Matching $[\text{Z}/\text{H}]$ instead of $[\text{Fe}/\text{H}]$ results in model colors that are substantially too red.

mean $\mu = 0.22$ and standard deviation $\sigma = 0.07$. There is no correlation between the corrected $\text{EW}([\text{OIII}])$ and galaxy σ , R_e , I_e , ΔI_e , age, $[\text{Fe}/\text{H}]$, $[\text{Mg}/\text{Fe}]$, or mismatch between the measured age and the closest BC03 model age.

We use the corrected $\text{EW}([\text{OIII}])$ measurements to estimate a correction to $\text{H}\beta$ using equation A1. These corrections are subtracted from the measured $\text{H}\beta$ line strengths. We then rerun the stellar population analysis on the corrected data. Correcting for emission infill produces ages that are ~ 0.12 dex lower than the uncorrected values, while $[\text{Fe}/\text{H}]$ values increase by ~ 0.06 dex.

These corrected ages are of course different from the original ages used to fit the BC03 models and measure $[\text{OIII}]$ emission. To check that the $\text{EW}([\text{OIII}])$ values are reasonable, we iterate the process, using the corrected ages to fit BC03 models to the stacked spectra and remeasure $\text{EW}([\text{OIII}])$. The resulting values of $\text{EW}([\text{OIII}])$ are typically 0.02 \AA smaller (with standard deviation 0.02 \AA) than the original estimate, which translates into $\text{H}\beta$ differences of < 0.015 . These differences are negligible.

COMPARING OBSERVED AND MODELED GALAXY COLORS

By comparing the color estimates from Figure 4b to the observed galaxy colors, we can check that this method of matching BC03 models to the data gives reasonable estimates of the stellar population properties of the sample galaxies. The spectroscopic data sample only the region of the galaxy covered by the SDSS spectral fibers, but many galaxies show significant color gradients. We therefore compare the predicted model $g-r$ colors from the spectroscopic data to the observed galaxy colors *as measured from SDSS photometry matched to the $3''$ SDSS spectral fiber aperture*. The fiber magnitudes are downloaded from the SDSS Catalog Archive Server¹⁹ and K-corrected to $z = 0$. We use the median value of the $g-r$ fiber color from all the constituent galaxies in the corresponding bin to determine the “observed” $g-r$ fiber color of each stacked spectrum.

Figure 15a shows the comparison between the observed $g-r$ fiber colors and those derived from the spectroscopic single burst models using the curves in Figure 4b. The various colors indicate the values of σ in each bin, as labelled. The solid line shows a one-to-one relation between observed and modeled colors, with the shaded region showing the typical 1σ error on the model colors as propagated through the stellar population modeling. Bins whose stacked spectra have considerably lower S/N (i.e., errors in the model colors more than twice as large) than the typical bins are shown as open circles. For the high- σ galaxies, the model colors are an excellent match to the observed colors. The observed colors are offset not more than 0.02 dex redder than the model colors derived for these galaxies, which may indicate low-level internal dust reddening within the sample galaxies. No reddening has been applied to the models.

At lower values of σ , the discrepancy between observed and modeled colors increases; the galaxies are observed to be 0.03–0.04 dex redder than the model colors. This systematic trend, wherein the models predict colors for the bluest galaxies that are systematically too blue, highlights the probable bias inherent in using single burst models. The Balmer absorption lines are highly sensitive to a small “frosting” of young stars—more so than the total galaxies

¹⁹ <http://cas.sdss.org/dr6/en/>

colors—and will therefore give age estimates that are systematically younger than models with composite star formation histories. These will then lead to predicted colors that are too blue and, as we show in section 4, to $M_{\star,IMF}/L$ values that are too low.

Given these considerations, the colors derived from the modelling illustrated in Figure 4 appear to do an excellent job of matching the observed galaxy colors. Furthermore, they reveal the effect of an expected systematic bias in the modeling process.

A further important issue is also clarified by matching the model and observed colors. The BC03 models are constrained to use the solar abundance ratios at all metallicities. However, massive early type galaxies are known to have super-solar enhancements of a number of elements, including Mg (e.g., Worthey et al. 1992) and C and N (e.g., Graves et al. 2007; Smith et al. 2009). Since a mismatch between the galaxy abundance patterns and the model abundance patterns is therefore inevitable, it is not obvious *a priori* whether one should attempt to match $[Fe/H]$ between the data and the models, or whether it would be more appropriate to match total metallicity ($[Z/H]$).

Figure 15a was constructed by matching $[Fe/H]$ between the data and the models. Figure 15b shows results when the match is instead based on $[Z/H]$. For the observed galaxies, $[Z/H]$ is calculated based on the assumption that the α -elements O, Ne, Na, Si, S, and Ti all track Mg, that the Fe-peak elements Cr, Mn, Co, Ni, Cu, and Zn all track Fe, and that Mg, Fe, C, N, and Ca have the abundances measured using EZ_Ages. All other elements are assumed to have solar abundances (see Graves et al. 2007, section 5.3).

Matching models to the data on the basis of $[Z/H]$ clearly does not do as well as matching based on $[Fe/H]$. The modeled colors are substantially redder than the observed colors for the high- σ galaxies.

The good match achieved between the observed and modeled colors using $[Fe/H]$ motivates us to use the same models to measure $M_{\star,IMF}/L$. We do this in section 4.1, keeping in mind the caveat that single burst models tend to produce colors that are too blue for the bluest galaxies and will similarly underestimate $M_{\star,IMF}/L$ for the lowest $M_{\star,IMF}/L$ galaxies.